Global Biogeochemical Cycles®

RESEARCH ARTICLE
10.1029/2023GB007986

Integrating Trait-Based Stoichiometry in a Biogeochemical Inverse Model Reveals Links Between Phytoplankton Physiology and Global Carbon Export

Megan R. Sullivan[1], François W. Primeau[1], George I. Hagstrom[2], Wei-Lei Wang[3], and Adam C. Martiny[1,4]

[1]Department of Earth System Science, University of California Irvine, Irvine, CA, USA, [2]Department of Ecology and Evolutionary Biology, Princeton University, Princeton, NJ, USA, [3]State Key Laboratory of Marine Environmental Science, College of Ocean and Earth Sciences, Xiamen University, Xiamen, China, [4]Department of Ecology and Evolutionary Biology, University of California Irvine, Irvine, CA, USA

Key Points:

- New framework embeds a mechanistic cellular growth model for phytoplankton stoichiometry in a global biogeochemical inverse model
- Four parameterizations of phytoplankton C:P ratios are optimized globally using an inverse model and multiple biogeochemical tracers
- Modeled C:P patterns impact global carbon export flux by 10%, with larger regional differences, and affect sensitivity to future change

Supporting Information:

Supporting Information may be found in the online version of this article.

Correspondence to:

M. R. Sullivan,
meganrs@uci.edu

Citation:

Sullivan, M. R., Primeau, F. W., Hagstrom, G. I., Wang, W.-L., & Martiny, A. C. (2024). Integrating trait-based stoichiometry in a biogeochemical inverse model reveals links between phytoplankton physiology and global carbon export. *Global Biogeochemical Cycles*, *38*, e2023GB007986. https://doi.org/10.1029/2023GB007986

Received 27 SEP 2023
Accepted 13 FEB 2024

Author Contributions:

Conceptualization: Megan R. Sullivan, François W. Primeau, Adam C. Martiny
Data curation: Megan R. Sullivan
Formal analysis: Megan R. Sullivan
Funding acquisition: François W. Primeau, Adam C. Martiny
Investigation: Megan R. Sullivan
Methodology: Megan R. Sullivan, François W. Primeau, George I. Hagstrom, Wei-Lei Wang, Adam C. Martiny
Resources: François W. Primeau
Software: Megan R. Sullivan, George I. Hagstrom, Wei-Lei Wang
Supervision: François W. Primeau, Adam C. Martiny

Abstract The elemental ratios of carbon, nitrogen, and phosphorus (C:N:P) within organic matter play a key role in coupling biogeochemical cycles in the global ocean. At the cellular level, these ratios are controlled by physiological responses to the environment. But linking these cellular-level processes to global biogeochemical cycles remains challenging. We present a novel model framework that combines knowledge of phytoplankton cellular functioning with global scale hydrographic data, to assess the role of variable carbon-to-phosphorus ratios ($R_{C:P}$) on the distribution of export production. We implement a trait-based mechanistic model of phytoplankton growth into a global biogeochemical inverse model to predict global patterns of phytoplankton physiology and stoichiometry that are consistent with both biological growth mechanisms and hydrographic carbon and nutrient observations. We compare this model to empirical parameterizations relating $R_{C:P}$ to temperature or phosphate concentration. We find that the way the model represents variable stoichiometry affects the magnitude and spatial pattern of carbon export, with globally integrated fluxes varying by up to 10% (1.3 Pg C yr^{-1}) across models. Despite these differences, all models exhibit strong consistency with observed dissolved inorganic carbon and phosphate concentrations ($R^2 > 0.9$), underscoring the challenge of selecting the most accurate model structure. We also find that the choice of parameterization impacts the capacity of changing $R_{C:P}$ to buffer predicted export declines. Our novel framework offers a pathway by which additional biological information might be used to reduce the structural uncertainty in model representations of phytoplankton stoichiometry, potentially improving our capacity to project future changes.

Plain Language Summary Phytoplankton play a vital role in Earth's carbon cycle. The ratios of carbon, nitrogen, and phosphorus in these tiny marine plants influence how much carbon they absorb at the surface and export to the deep ocean. Yet, many models overlook the global variability of these ratios. Our study introduces an innovative model that combines microscopic knowledge of phytoplankton growth with global ocean data. We use this model to predict how the elemental ratios in phytoplankton vary on a global scale. By comparing this detailed model to simpler models based on individual environmental controls, we reveal that the way we represent these ratios significantly impacts carbon export patterns. Different representations of these ratios lead to estimates of carbon export from the ocean's surface that differ by over 1 billion tons annually. We also find that the flexibility of elemental ratios can counteract future declines in ocean productivity to varying degrees, depending on the assumed environmental controls of these ratios. Our findings highlight the critical role of understanding the connection between phytoplankton elemental composition and their environment and underscore the need for improved models to better anticipate future changes in the ocean's carbon cycle.

1. Introduction

The stoichiometry of carbon, nitrogen, and phosphorus (C:N:P) within organic matter plays a crucial role in coupling biogeochemical cycles in the global ocean. Biogeochemical models have historically assumed a fixed ratio of C:N:P = 106:16:1, known as the "Redfield" ratio, based on early observations of consistent stoichiometry between suspended organic matter and seawater (Redfield, 1934, 1958). While many global models still rely on fixed ratios (Séférian et al., 2020), stoichiometric variability has been increasingly recognized as an important control on biological carbon fluxes over the past decade (Galbraith & Martiny, 2015; Kwon, Sreeush, et al., 2022). The elemental ratios of phytoplankton link nutrient cycles and carbon fixation, thus impacting the distribution of

Validation: Megan R. Sullivan
Visualization: Megan R. Sullivan
Writing – original draft: Megan R. Sullivan
Writing – review & editing: Megan R. Sullivan, François W. Primeau, George I. Hagstrom, Wei-Lei Wang, Adam C. Martiny

organic carbon production and export to the deep ocean. In the latest generation of climate models, global particulate organic carbon (POC) export rates range widely, from 4.5 to 12 Pg C yr^{-1}, for the preindustrial era (Henson et al., 2022). This uncertainty arises from differing model representations of several processes that drive export, including inconsistent representations of phytoplankton stoichiometry (Henson et al., 2022; Kwiatkowski et al., 2018; Séférian et al., 2020). Observations of particulate organic matter (POM) in the surface ocean have revealed spatial patterns in C:P ratios ($R_{C:P}$), with higher ratios in warm, nutrient-limited regions and lower ratios in nutrient-replete regions, leading to enhanced or diminished carbon export, respectively (Martiny et al., 2013; Tanioka, Garcia, et al., 2022). The geographic variations in $R_{C:P}$ of phytoplankton and exported organic matter could significantly impact the long-term distribution of carbon pools between the atmosphere and ocean. Environmentally driven shifts in organic matter stoichiometry may buffer decreases in biological carbon uptake under future climate scenarios (Tanioka & Matsumoto, 2017). For instance, increasing phosphorus use efficiency has been shown to compensate for declining nutrient inputs, leading to stable carbon export at the Bermuda Atlantic Time-series Site despite warming, increased stratification, and reduced nutrient supply in recent years (Lomas et al., 2022). A number of modeling studies have shown that increasing phytoplankton nutrient use efficiency could buffer expected future declines in carbon export (Kwiatkowski et al., 2018; Kwon, Sreeush, et al., 2022; Tanioka & Matsumoto, 2017). However, the magnitude of this buffering effect is uncertain and could range from a small effect (Kwiatkowski et al., 2018; Tanioka & Matsumoto, 2017) to entirely offsetting the effects of diminished surface nutrients to maintain relatively constant carbon export by the end of the 21st century (Kwon, Sreeush, et al., 2022). Therefore, accurately accounting for stoichiometric variability is essential for understanding how ocean carbon and nutrient cycles respond to environmental change.

While phytoplankton stoichiometry plays a crucial role in the biological carbon pump, parameterizing stoichiometry in global models remains a challenge, as there is no clear consensus on the dominant mechanism driving global variability. Fixed stoichiometry continues to be used widely in biogeochemical models (Henson et al., 2022; Séférian et al., 2020). The global models that have transitioned to variable stoichiometry typically rely on simple empirical relationships between $R_{C:P}$ and environmental conditions instead of explicitly modeling the underlying physiological mechanisms controlling $R_{C:P}$ (e.g., Long et al., 2021; Moore et al., 2013). Multiple hypotheses could explain how environmental conditions drive varying C:P ratios in phytoplankton (see review by Moreno and Martiny (2018)). For example, the translation-compensation hypothesis posits that global patterns of C:P ratios are primarily driven by temperature. This hypothesis assumes the total phosphorus requirement of a cell is controlled primarily by the cellular content of phosphorus-rich ribosomes. This is based on the idea that the synthesis rate of ribosome-specific proteins is temperature-sensitive, so cells require higher ribosome content at lower temperatures to achieve the same growth rate (Toseland et al., 2013; Yvon-Durocher et al., 2015). Another hypothesis suggests that phytoplankton decrease intracellular phosphorus demand under phosphorus-limited conditions, for example, by substituting phospholipids with sulpholipids (Lin et al., 2016; Van Mooy et al., 2009). Due to the covariation of temperature and nutrient availability on large scales and the limited data set of in situ measurements, the relative influence of these different environmental factors remains unclear (Tanioka, Garcia, et al., 2022). Because the dominant driver remains ambiguous, empirical models differ in how they link the environment to stoichiometry. Proposed models include simple functions of temperature (e.g., Yvon-Durocher et al., 2015), nutrients (e.g., Galbraith & Martiny, 2015), or a combination of multiple environmental factors (e.g., Tanioka, Garcia, et al., 2022). However, all of these models lack a mechanistic link to biological processes that control phytoplankton composition, which can limit their predictive power, particularly under novel or changing environmental conditions. Furthermore, these empirical relationships are derived from suspended POM observations, which may not be representative of the organic matter exported from the euphotic zone. To predict future changes to the biological carbon export flux, it is necessary to understand the mechanistic links between observed variables and the stoichiometry of exported material.

The combination of a trait-based mechanistic model of phytoplankton growth and a global biogeochemical inverse model presents a novel framework for investigating the underlying mechanisms driving global patterns of C:P ratios. Recent advances in inverse modeling have enabled the prediction of global patterns of exported organic matter C:P ratios using extensive biogeochemical tracer observations (e.g., phosphate and dissolved inorganic carbon) combined with a data-constrained ocean circulation model. By optimizing a biogeochemical inverse model across 11 ocean provinces, Teng et al. (2014) found regionally distinct $R_{C:P}$ values which aligned well with the patterns seen in surface POM observations. Kwon, Holzer, et al. (2022) extended the inverse modeling framework to constrain how C:P ratios covary with sea surface phosphate concentrations. Building

upon these advancements and drawing upon recent progress in computational ecology, we further develop the inverse-modeling framework by incorporating biological mechanisms that drive C:P ratios globally. This integration represents a novel combination of cellular-level processes with global-scale hydrographic data, accounting for the joint uncertainty of hydrographic and biological observations. Our approach embeds a trait-based mechanistic model of phytoplankton growth into a global steady-state biogeochemical inverse model. Trait-based approaches, which define the phytoplankton community in terms of cellular-level physiological traits that trade-off in response to different environmental conditions, are increasingly common in community ecology (Kiørboe et al., 2018; Litchman & Klausmeier, 2008). Our trait-based cellular growth model relates phytoplankton growth, elemental stoichiometry, and environmental factors including light, temperature, and nutrient availability. We use an optimality-based approach (Smith et al., 2011), in which cellular growth rates are maximized by reallocating resources to different functional or macromolecular pools under given growth conditions (e.g., Daines et al., 2014; Inomura et al., 2020; Moreno et al., 2018). To avoid any sampling bias that could be reflected in observations of suspended particulate organic matter, we optimize the cellular growth model using only the imprint of cellular stoichiometry on the global hydrographic tracer fields. This approach allows us to predict global patterns of phytoplankton stoichiometry and biological carbon export that are jointly consistent with both hydrographic observations and biological growth mechanisms.

Here, we assess the impacts of different $R_{C:P}$ parameterizations on the global total organic carbon export flux and the capacity for changes in phytoplankton $R_{C:P}$ to buffer predicted declines in export production. To do this, we optimize a steady-state biogeochemical inverse model using a variety of parameterizations for phytoplankton $R_{C:P}$. This includes a globally constant $R_{C:P}$ parameter as a baseline of comparison, as well as two simple empirical functions of the environment: (a) a hyperbolic function of temperature and (b) a hyperbolic function of phosphate concentration. Next, to address the lack of mechanistic basis of these simple empirical models, we implement a more complex mechanistic cellular growth model to determine the spatial pattern of $R_{C:P}$. We investigate how the cellular growth model can provide a more mechanistic understanding of the emergent $R_{C:P}$ patterns than empirical models and demonstrate the potential of using hydrographic observations to constrain a generalizable model of cellular-scale phytoplankton growth. Finally, we test the sensitivity of the carbon cycle to the predicted $R_{C:P}$ patterns under a hypothetical future climate. Overall, our findings emphasize the critical role of accurately representing phytoplankton stoichiometry in global biogeochemical models.

2. Methods

We optimize a biogeochemical inverse model using each of the four parameterizations for organic matter $R_{C:P}$ described below. The optimizable parameters are summarized in Table 2. The inverse model optimization, described in Section 2.2, finds the parameter set that produces the best possible fit to climatological mean hydrographic observations. We next project these models under an idealized future climate scenario to demonstrate the effect of different $R_{C:P}$ parameterizations on predictions of future carbon export and atmospheric pCO_2.

2.1. Stoichiometric Models

2.1.1. Constant Model

To establish a baseline of comparison, we optimize the biogeochemical inverse model using a globally constant value for organic matter $R_{C:P}$. This stoichiometric model adds a single optimizable parameter, $r_{C:P}^{\text{const}}$, to the base biogeochemical model (described in Section 2.2 and Appendix A).

2.1.2. Phosphate-Only Model

The nutrient-only stoichiometric model is based on the $R_{P:C}$ regression of Galbraith and Martiny (2015). This model expresses phytoplankton $R_{C:P}$ as a hyperbolic function of the ambient phosphate concentration:

$$R_{C:P} = \frac{1}{c_1[\text{DIP}]_{\text{obs}} + c_2}, \tag{1}$$

where c_1 and c_2 are optimizable parameters, and $[\text{DIP}]_{\text{obs}}$ is the climatological observed phosphate concentration field from the World Ocean Atlas 2013 (H. E. Garcia et al., 2014). In this model, the reciprocal of $R_{C:P}$, phytoplankton $R_{P:C}$, is a linear function of phosphate. Using the observed [DIP], rather than the modeled [DIP], in

the $R_{C:P}$ parameterization allows us to circumvent potential errors stemming from bias in modeled surface phosphate concentrations.

2.1.3. Temperature-Only Model

The temperature-only stoichiometric model expresses phytoplankton $R_{C:P}$ as a hyperbolic function of temperature:

$$R_{C:P} = \frac{1}{c_3 T_{\text{obs}} + c_4}, \tag{2}$$

where c_3 and c_4 are optimizable parameters. This functional form was chosen for ease of comparison with the nutrient-only model. T_{obs} in this equation is the climatological observed temperature from World Ocean Atlas 2013 (Locarnini et al., 2013). In this model $R_{P:C}$ is a linear function of temperature.

2.1.4. Mechanistic Cellular Growth Model

The mechanistic stoichiometric model is a trait-based model of phytoplankton growth that expresses phytoplankton $R_{C:P}$ as a non-linear function of four environmental variables: temperature, phosphate concentration, nitrate concentration, and photosynthetically active radiation (PAR). As in the temperature-dependent and phosphate-dependent model, these environmental variables are set to the World Ocean Atlas gridded climatological mean fields for temperature (Locarnini et al., 2013) and nutrient concentrations (H. E. Garcia et al., 2014), as well as a satellite-based estimate of euphotic zone PAR (NASA, 2018). Since we do not explicitly model a nitrogen cycle, utilizing the observed dissolved inorganic phosphorus (DIP) concentrations in the $R_{C:P}$ parameterization, instead of relying on modeled [DIP], both prevents the propagation of biases in the surface DIP field and ensures a realistic degree of covariance with the observed distribution of surface DIN concentrations. The inverse model optimization, described in the following Section 2.2, optimizes five adjustable parameters within this model (summarized in Table 2). The remaining fixed parameter values are listed in the appendix Table B1.

In this model, the phytoplankton C:P ratio is calculated as the ratio between cellular quotas of carbon, QC_{cell}, and phosphorus, QP_{cell}, such that

$$R_{C:P} = \frac{QC_{\text{cell}}}{QP_{\text{cell}}}. \tag{3}$$

The full expression for the quotas, QP_{cell} and QC_{cell}, are shown in Equations 11 and 14. In our resource allocation model, these cellular quotas are determined by optimizing the relative allocation of cellular dry mass to specific functional apparatuses, each with fixed carbon and phosphorus content, in order to maximize growth rates in a given environment. This model, based on the works of Shuter (1979) and expanded by Moreno et al. (2018), captures essential physiological constraints and trade-offs governing cellular growth in response to environmental variations. Phytoplankton adapt to resource limitations by reallocating metabolic resources among different cellular functions to optimize growth (Geider & La Roche, 2002; Moreno & Martiny, 2018). The model represents a trade-off between investment in photosynthesis, biosynthesis, and nutrient acquisition.

The total dry mass of a cell with radius r is divided into fractional contributions to a set of functional pools: the photosynthetic apparatus (L), the biosynthetic apparatus (E), and structural components ($S(r)$). The allocations to these pools must satisfy:

$$L + E + S(r) = 1. \tag{4}$$

Each functional compartment has a fixed stoichiometry, calculated by the weighted average stoichiometry of the primary macromolecules (e.g., proteins, lipids, ribosomes, DNA) making up the compartment. Approximate values for the elemental composition of each class of macromolecule are taken from Geider and La Roche (2002) and listed in Table 1. We assume that 60% of the biosynthetic apparatus is composed of ribosomes, with proteins making up the remaining 40% of this pool, and that 70% of the photosynthetic apparatus is composed of proteins with the remaining 30% of this pool composed of lipids.

The structural compartment includes cell membrane, nutrient uptake proteins, and a fixed allocation, γ_S, to other necessary structural components such as DNA and other lipids that are not involved in photosynthesis or biosynthesis,

$$S(r) = \frac{\alpha_S}{r} + \gamma_S. \tag{5}$$

The specific allocation to surface-associated structure (i.e., machinery associated with the membrane and periplasmic space), α_S/r, is inversely proportional to cell size to account for the changing relative volume of a cell's surface structure with radius (following Clark et al. (2011) and Clark et al. (2013)). For simplicity, we assume the mass allocated to this pool is divided evenly between membrane and periplasm/nutrient uptake machinery. We prescribe the specific allocation to the size-independent structural pool as $\gamma_S = 0.189$.

The cellular growth rate is determined by the minimum of the mass-specific photosynthetic, biosynthetic, and nutrient (P & N) uptake rates

$$\mu_L = \frac{\alpha_I L}{1 + \Phi_S}, \tag{6}$$

$$\mu_E = k_{ST} E, \tag{7}$$

$$\mu_P = \frac{4\pi r f_P D_P [\mathrm{DIP}]}{\frac{4}{3}\pi r^3 \rho_{\mathrm{cell}}\, p_{\mathrm{dry}} \left(E P_E + \gamma_S P_S\right)}, \tag{8}$$

$$\text{and,} \quad \mu_N = \frac{4\pi r D_N [\mathrm{DIN}]}{\frac{4}{3}\pi r^3 \rho_{\mathrm{cell}}\, p_{\mathrm{dry}} \left(E N_E + L N_L + \gamma_S N_S + \frac{\alpha_S}{2r}\left(f_P N_{prot} + N_{mem}\right)\right)}. \tag{9}$$

The maximum photosynthetic and biosynthetic rates are proportional to the investment in the respective functional pools, L and E. The specific rate of carbon fixation from photosynthesis, α_I, is a function of light and temperature. The light response is designed to capture the effects of both electron transport and carbon fixation on photosynthesis, following Moreno et al. (2018), and the temperature dependence is modeled as a Q_{10} function with an optimizable parameter, Q_{10}^{photo}, that is, $\alpha_I(T) = (\alpha_I)_{T_0} \times \left(Q_{10}^{\mathrm{photo}}\right)^{(T-T_0)/10}$. A fixed specific carbon cost of synthesis, $\Phi_S = 0.67$, is prescribed following Shuter (1979). The efficiency of biosynthesis (k_{ST}) depends on temperature with an optimizable reference value (k_{ST_0}) at 25°C and a prescribed Q_{10} value of 2 (Shuter, 1979). Nutrient uptake is assumed to be diffusion limited. The mass specific uptake rates of P and N are defined as the diffusive flux across the cell surface divided by the mass of the nutrient within all functional machinery in the cell. The diffusive flux scales with cell size and the ambient nutrient concentration ([DIP] or [DIN]). The diffusivity, D, is assumed to depend on temperature with a Q_{10} value of 1.5 and a reference diffusivity of 1.3×10^{-9} m^2/hr at 15°C. The intracellular nutrient content is determined by the total dry mass of the cell and the average mass fraction of the nutrient within all functional machinery, weighted by the allocation to each pool. In Equations 8 and 9, P_X and N_X denote the mass fraction of phosphorus and nitrogen in the functional pool, X, where X represents E, L, or S. Phosphorus uptake is further limited by the concentration of dedicated P uptake proteins (f_P) in the cell's periplasmic space. Under P limitation, all of the periplasmic mass is dedicated to uptake proteins. When phosphorus is not limiting, small cells can reduce their N requirement by reducing their investment in phosphate uptake proteins, down to a minimum concentration (A_{min}) of 5% of the cell dry mass, such that

$$\begin{aligned} \frac{2A_{\mathrm{min}} r}{\alpha_S} \le f_P \le 1, \quad & \text{if } r < \frac{\alpha_S}{2A_{\mathrm{min}}}, \\ f_P = 1, \quad & \text{otherwise.} \end{aligned} \tag{10}$$

The model finds the cellular strategy (i.e., chooses values for E, L, r, and f_P), that maximizes the growth rate in a given environment. We assume that this strategy represents the dominant phenotype of the local phytoplankton community, and is therefore representative of the entire community.

Since the mass-specific nutrient uptake rates scale with $1/r^2$, smaller cells have higher nutrient affinities, providing a competitive advantage for small cells in nutrient-limited regions. Where nutrients are replete, larger

Table 1
Approximate Elemental Composition of the Macromolecules Represented in the Cellular Growth Model, Expressed as the Mass of Each Element With Respect to the Molecules Dry Weight[a]

Molecule	Composition	gC/gDW	gN/gDW	gP/gDW
Protein	$C_{4.43}H_7O_{1.44}N_{1.16}S_{0.019}$	0.53	0.16	–
Lipids	$C_{40}H_{74}O_5$	0.76	–	–
Phospholipids	$C_{37.9}H_{72.5}O_{9.4}N_{0.43}P$	0.65	0.008	0.043
Ribosomes[b]	RNA + Protein	0.419	0.16	0.047
DNA	$C_{9.75}H_{14.25}O_8N_{3.75}P$	0.36	0.16	0.095

[a]Values compiled by Geider and La Roche (2002). [b]Assumes ribosomes are composed of equal amounts RNA and proteins.

cells are able to achieve faster maximum growth rates by increasing their relative allocations to L and E (Equations 6 and 7). Thus there is a trade-off between nutrient affinity and maximum growth rate. The optimal solution balances rates of nutrient uptake, biosynthesis, and photosynthetic carbon fixation ($\mu_E = \mu_L = \mu_{nutrient}$). The nutrient limitation will be either N limited ($\mu_{nutrient} = \mu_N < \mu_P$ with f_P minimized), P limited ($\mu_{nutrient} = \mu_N < \mu_P$ with $f_P = 1$), or co-limited ($\mu_{nutrient} = \mu_N = \mu_P$), depending on the environmental conditions.

Once the allocation to each functional pool is determined, $R_{C:P}$ is calculated by dividing the cellular C quota by the cellular P quota. The cellular P quota is determined by the percentage of cellular dry mass that is allocated to each functional pool containing phosphorus, that is, biosynthesis and size-independent structure. The model also allows for cellular inorganic phosphorus (e.g., polyphosphate) accumulation in large cells. Inorganic phosphorus storage within cells is poorly understood and difficult to quantify (Martin & Van Mooy, 2013), so it is currently parameterized simply to scale as a logistic function of ambient phosphate, with coefficients that must be determined empirically. Additionally, the phospholipid content can be modulated to account for sulfolipid substitution at low phosphate concentrations (Van Mooy et al., 2009). The total cellular P quota is calculated as

$$QP_{\text{cell}} = \frac{4}{3}\pi r^3 \rho_{\text{cell}} p_{\text{dry}} \left(\frac{EP_E + \gamma_S P_S}{m_P} + QP_{\text{phospholipid}} + QP_{\text{storage}} \right), \quad (11)$$

where the product of the cell volume $\left(\frac{4}{3}\pi r^3\right)$, cell density ($\rho_{\text{cell}}$), and dry mass fraction of the cell (p_{dry}) yields the total dry mass of the cell. P_E and P_S are the mass fraction of phosphorus in the biosynthetic and size-independent structural functional pools, respectively, and $m_P = 31.0$ g/mol is the molar mass of phosphorus. In our model, phospholipids and phosphorus storage are treated as non-essential phosphorus pools, and are modeled as,

Table 2
Optimized Parameter Descriptions and Units

Symbol	Description	Units
b_P	Martin curve exponent of POP flux attenuation profile	–
k_{dP}	DOP remineralization rate constant	s^{-1}
α	Coefficient for NPP (Equation A6)	s^{-1}
β	Exponent for NPP (Equation A6)	–
b_C	Exponent of POC flux attenuation profile	–
d	e-folding length scale for PIC flux attenuation	m
k_{dC}	DOC remineralization rate constant	s^{-1}
R_{rain}	Rain ratio ($CaCO_3$ to POC production ratio)	–
$r_{C:P}^{\text{const}}$	Globally Constant $R_{C:P}$ value	molC/molP
c_1	Coefficient of [DIP] in Equation 1	$\frac{\text{molP}}{\text{molC}}\mu M^{-1}$
c_2	Constant coefficient in Equation 1	molP/molC
c_3	Coefficient of Temperature in Equation 2	$\frac{\text{molP}}{\text{molC}}(°C)^{-1}$
c_4	Constant coefficient in Equation 2	molP/molC
Q_{10}^{photo}	Q10 Temperature dependence of photosynthesis	–
f_{stor}	Scale factor for intracellular phosphorus storage	$\frac{\text{molP}}{\text{molC}}\mu M^{-1}$
$k_{S,T0}$	Synthesis rate of biosynthetic apparatus at 25°C	hr^{-1}
r_0^{stor}	Size threshold for P storage (inflection point of the logistic function in Equation 13)	μm
α_S	Proportionality coefficient that scales surface-associated structure with cell size	μm

$$QP_{\text{phospholipid}} = QC_{\text{cell}} \frac{f_{\text{plip}} \frac{\alpha_S}{2r} P_{\text{plip}} \left(\frac{m_C}{m_P}\right)}{1 + e^{-\beta_{\text{plip}}([\text{DIP}] - [\text{DIP}]_0^{\text{plip}})}}, \tag{12}$$

and

$$QP_{\text{storage}} = QC_{\text{cell}} \frac{f_{\text{stor}} [\text{DIP}]}{1 + e^{-\beta_{\text{stor}}(r - r_0^{\text{stor}})}}. \tag{13}$$

The maximum phospholipid content of the cell is inversely proportional to r, so the maximum potential contribution of phospholipids to the total cellular phosphorus quota increases for smaller cells, and this term becomes negligible for sufficiently large cells. The modeled phospholipid content is scaled following a logistic function of the ambient phosphate concentration with midpoint $[\text{DIP}]_0^{\text{plip}} = 1$ mmol m^{-3} and scale factor $\beta_{\text{plip}} = 3$ m^3 mmol^{-1}. In Equation 13, f_{stor} is an optimizable parameter that scales phosphorus storage linearly with the ambient phosphate concentration. Intracellular phosphorus storage approaches this linear relationship when cells are large $\left(r > r_0^{\text{stor}}\right)$ and approaches zero as cell size decreases for $r < r_0^{\text{stor}}$. The inflection point of the logistic function sigmoid, denoted as r_0^{stor}, is an optimizable parameter that signifies the size threshold below which the storage quota approaches zero. Additionally, the scale factor, $\beta_{\text{stor}} = 2$ μm^{-1}, governs the size range over which the function transitions from near zero to asymptotically approaching a linear function of phosphate. Equations 12 and 13 are formulated to be consistent with Equation 21 of Moreno et al. (2018), in which $R_{C:P} = 1/\left(R_{P:C}^{\text{functional}} + R_{P:C}^{\text{storage}}\right)$.

The cellular carbon quota is determined by the percentage of cellular dry mass that is allocated to each functional pool containing carbon, as well as a carbon reserve pool. The C quota is calculated as,

$$QC_{\text{cell}} = \frac{4}{3}\pi r^3 \rho_{\text{cell}} p_{\text{dry}} \frac{\left(EC_E + LC_L + \gamma_S C_S + \frac{\alpha_S}{2r}\left(f_P C_{prot} + C_{mem}\right)\right)}{m_C}\left(1 + f_{\text{Creserve}}\right), \tag{14}$$

where C_E C_L and C_S are the mass fraction of carbon in the biosynthetic, photosynthetic, and size-independent structural pools, respectively; C_{prot} and C_{mem} are the mass fraction of carbon in nutrient uptake proteins and cell membrane; $m_C = 12.0$ g/mol is the molar mass of carbon, and the relative amount of cellular carbon stored in the carbon reserve is controlled by,

$$f_{\text{C reserve}} = \frac{24}{4}\mu_L(1 + \Phi_S) = \kappa\alpha_I L. \tag{15}$$

The size of this carbon reserve is proportional to the growth rate of the cell. Excess carbon is accumulated in this reserve by photosynthesis throughout the day to sustain the carbon cost of cellular maintenance during the night. The factor of 1/4 in Equation 15 comes from integrating the photosynthetic carbon fixation rate over a 24 hr period, assuming a fixed diurnal cycle with 12 hr of light daily.

2.2. Inverse Modeling Method

The global biogeochemical model solves for the steady-state phosphorus and carbon cycles. The phosphorus cycle model resolves three pools: dissolved inorganic phosphorus (DIP), dissolved organic phosphorus (DOP), and particulate organic phosphorus (POP). The carbon cycle model has four pools: dissolved inorganic carbon (DIC), dissolved organic carbon (DOC), particulate organic carbon (POC), as well as particulate inorganic carbon (PIC) in the form of calcium carbonate. Additionally, the carbon cycle model includes tracers for alkalinity and, optionally, atmospheric pCO_2. The model utilizes a data-constrained 3D advection-diffusion operator computed with the Ocean Circulation Inverse Model (OCIM; DeVries & Holzer, 2019; DeVries & Primeau, 2011). The circulation model has a horizontal resolution of 2° × 2° with 24 layers ranging in thickness from 36 m near the surface to 633.5 m near the bottom. Using the pre-computed transport matrix from OCIM allows us to efficiently solve the governing biogeochemical equations while maintaining realistic ocean circulation patterns.

The governing equations for the phosphorus and carbon cycle models are shown in Appendix A. In both biogeochemical cycles, particulate organic matter (POP and POC) is formed by the assimilation of inorganic

tracers (DIP and DIC); particulate organic matter dissolves into DOP and DOC, and these dissolved organic tracers remineralize to form DIP and DIC. Particulate organic matter (POM) is produced in the euphotic zone, defined as the top two vertical layers of the model, spanning from the sea surface to a globally constant depth of 73.4 m. The biological uptake rate is modeled using satellite-based estimates of net primary production (NPP) and scaled by two optimizable parameters, α and β (Equation A6). We assume all production is fueled by DIP assimilation, neglecting any biological uptake of dissolved organic matter (DOM). Although we do not explicitly model other limiting nutrients (e.g., N, Fe, Si), their influence is implicit in the production term through the impact of nutrient limitation on the spatial variability of the observed NPP field. The net production of organic carbon is assumed to be proportional to organic phosphorus production with a spatially variable stoichiometric ratio, $R_{C:P}$, described in the stoichiometric models Section 2.1. For simplicity, all POM production is routed through the particulate pool before dissolving into DOM and remineralizing. This simplified routing differs from other biogeochemical models, in which net production feeds into both POM and DOM, and the remineralization of both POM and DOM influences their inorganic pools. We chose this simplified routing of organic matter through the particulate and dissolved pools because previous inverse modeling studies by Kwon, Holzer, et al. (2022) and Wang et al. (2019) found that the POM and DOM partitioning of net community production are weakly constrained by the inverse model. This is largely due to the coarse resolution of our model. At the resolution of our model, the net effect of either regeneration pathway is effectively equivalent. The inverse model balances the net production of a tracer within a grid box with the flux divergence of that tracer out of the grid box. Because biological transformations operate on shorter timescales than circulation, achieving this balance is insensitive to the specific production or remineralization pathway organic matter follows within a grid box. Additionally, biogenic production of PIC is proportional to POC production, using a globally uniform rain ratio (R_{rain}; optimizable parameter). PIC remineralizes directly to DIC with a prescribed dissolution rate constant, and the sinking flux of PIC attenuates following an exponential function with a globally uniform dissolution length scale (d; optimizable parameter). Globally uniform parameters control the dissolution rate of POM (κ_p; fixed parameter) and remineralization rate of DOM (k_{dP} and k_{dC}; optimizable parameters). The sinking flux of POM attenuates according to a power law function with a globally constant exponent. To allow for preferential remineralization of organic phosphorus, the model optimizes separate exponents for POP (b_P) and for POC (b_C). While vertical migration is not explicitly represented, it is implicitly accounted for in the model, as migratory export influences the shape of the POP and POC flux-attenuation profiles.

The phosphorus cycle model can be solved for the steady-state [DIP], [DOP], and [POP] fields by direct matrix inversion. Given the [DIP] solution, the carbon cycle model is solved iteratively using Newton's method (Kelley, 2003). The steady-state solutions to the governing equations yield the biogeochemical tracer fields expressed as implicit functions of the model's adjustable parameters. The log-transformed adjustable parameters are optimized using Matlab's unconstrained optimization function, `fminunc`, to minimize the negative of the log of the posterior probability function (i.e., to minimize the misfit between the model solution and the climatological average observed tracer fields). Because we assign flat priors to the parameters to be optimized, this objective function is equivalent to the negative log likelihood function, assuming Gaussian errors. This objective function measures the fraction of the observed variances in the climatological mean DIP, DIC, DOC, and alkalinity tracer fields that the model is unable to capture.

For our comparison of $R_{C:P}$ parameterizations, we first optimize the phosphorus cycle model to the climatological mean DIP observations, obtained from GLODAPv2 (Olsen et al., 2016) and regridded to our model grid. We optimize four adjustable parameters in the phosphorus cycle model: k_{dP}, b_P, α, and β (Table 2). The objective function to be minimized is the negative of the logarithm of the posterior probability function (abbreviated as the log-improbability function, L_{imp}), defined as

$$L_{imp,P} = \frac{1}{2}\frac{\sum V \cdot \left([\mathrm{DIP}]_{\mathrm{mod}} - [\mathrm{DIP}]_{\mathrm{obs}}\right)^2}{\sum V \cdot \left([\mathrm{DIP}]_{\mathrm{obs}} - \langle [\mathrm{DIP}]_{\mathrm{obs}} \rangle\right)^2}, \tag{16}$$

where V is the volume of the model grid cells, the angle brackets represent the volume-weighted global average, and the subscripts mod and obs indicate modeled and observed fields. The modeled field is the steady-state solution to the phosphorus cycle model. In constructing this objective function, we extract only the model grid cells in which we have observations.

We then perform separate optimizations of the carbon cycle model, each with one of the four parameterizations of $R_{C:P}$ of biological uptake (described in Section 2.1). Table 2 provides a summary of all optimizable parameter descriptions. Regardless of the choice of $R_{C:P}$ parameterization, the model optimizes four carbon cycle parameters: b_C, k_{dC}, d, and R_{rain}. In addition to these four parameters, the constant $R_{C:P}$ model optimizes one parameter for the globally constant $R_{C:P}$ value, and the models with temperature-dependent and phosphate-dependent $R_{C:P}$ each optimize two additional parameters controlling the variability of $R_{C:P}$. The cellular growth model optimizes five additional parameters affecting $R_{C:P}$, bringing the total to nine optimizable parameter values for this model. The resulting models therefore differ in more than just the spatial pattern of $R_{C:P}$. This allows for some compensation between the pattern of $R_{C:P}$ and the magnitude of these carbon cycle parameters.

For this optimization the log-improbability function is defined as:

$$L_{imp,C} = \frac{1}{2}\left(\frac{\sum V\cdot\left(\left([\mathrm{DIC}]_{\mathrm{mod}} + \mathrm{C_{ant}}\right) - [\mathrm{DIC}]_{\mathrm{obs}}\right)^2}{\sum V\cdot\left([\mathrm{DIC}]_{\mathrm{obs}} - \langle[\mathrm{DIC}]_{\mathrm{obs}}\rangle\right)^2} + \frac{\sum V\cdot\left([\mathrm{ALK}]_{\mathrm{mod}} - [\mathrm{ALK}]_{\mathrm{obs}}\right)^2}{\sum V\cdot\left([\mathrm{ALK}]_{\mathrm{obs}} - \langle[\mathrm{ALK}]_{\mathrm{obs}}\rangle\right)^2} + \frac{1}{4}\frac{\sum V\cdot\left([\mathrm{DOC}]_{\mathrm{mod}} - [\mathrm{DOC}]_{\mathrm{obs}}\right)^2}{\sum V\cdot\left([\mathrm{DOC}]_{\mathrm{obs}} - \langle[\mathrm{DOC}]_{\mathrm{obs}}\rangle\right)^2}\right). \quad (17)$$

As in the phosphorus model, V is the volume of the model grid cells and the angle brackets represent the volume-weighted global averages for the tracers. The subscripts mod and obs refer to the steady-state solution to the carbon cycle model and observed tracer fields, respectively. The DIC and alkalinity observations are from the GLODAPv2 data set (Olsen et al., 2016) and the DOC observations are from a global compilation by Letscher and Moore (2015), in which the refractory component has been removed. The observations in these data sets are bulk-averaged onto our model grid. We assign a weighting factor for DOC that is 25% of the other components because there are larger observational uncertainties for DOM compared to the mapped DIC and alkalinity fields. Additionally, there are significantly fewer DOC observations than observations of DIC and ALK: after binning, we have 63,211 independent DIC data points and 59,211 independent ALK data points, while the DOC compilation has only 9,505 independent data points.

In order to use contemporary DIC observations to constrain the preindustrial steady-state model, we need to account for the change in ocean DIC concentration due to anthropogenic CO_2 uptake. Therefore, we add an anthropogenic DIC field, C_{ant}, to the steady state solution, $[DIC]_{mod}$ in the objective function. This field is estimated by time-stepping the carbon cycle model from an initial preindustrial steady-state solution, using a prescribed atmospheric pCO_2 time-series (Meinshausen et al., 2017). We then define C_{ant} as the difference between the contemporary model DIC field and the steady state model solution. We assume the biological carbon pump does not change over the course of the observational record and that the impact of the biological model on the physical transport of injected anthropogenic DIC is negligible. We also assume that any differences in anthropogenic DIC uptake between biological models have negligible impact on air-sea gas exchange. Therefore, C_{ant} is computed once prior to model optimization and remains fixed across all model optimizations.

2.3. Testing Sensitivity to Future Change

After optimizing the biogeochemical model with each of the four parameterizations of $R_{C:P}$, we next explore how changing environmental conditions affect stoichiometric ratios and ocean carbon storage by reevaluating each of the optimized models for a hypothetical future climate. To isolate the direct effect of the temperature and/or nutrient dependence of stoichiometry, we performed an idealized sensitivity study in which we reevaluated the four $R_{C:P}$ functions given perturbed environmental inputs, and used the resulting spatial distribution of $R_{C:P}$ to recompute a new carbon cycle equilibrium state. All model parameters were held fixed to the values optimized for the preindustrial ocean state. We applied globally uniform perturbations to the temperature and nutrient fields seen by the $R_{C:P}$ functions. Surface phosphate and nitrate concentrations were reduced by 31% and 21% respectively, based on the relative change in the global mean surface nutrient concentrations between 1850 and 2100, predicted by a global climate model (CESM) under the RCP8.5 emissions scenario. Using a relative change rather than modeled projections directly ensures that the direction of change from the historical observations is consistent with the direction of change predicted by the climate model and ensures reasonable projected concentrations, despite biases in the climate model's preindustrial state. We additionally increase the surface ocean

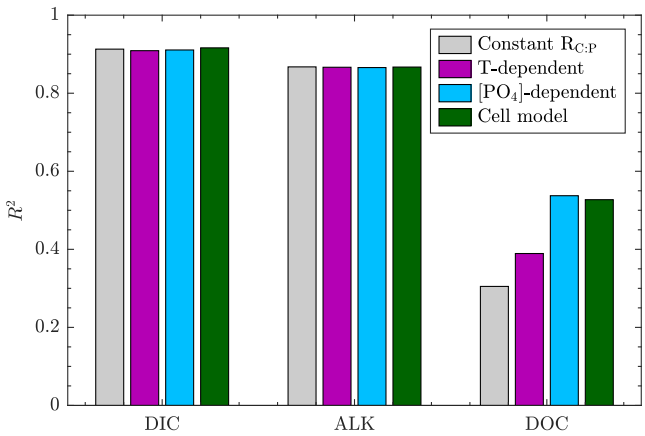

Figure 1. Coefficient of determination, R^2, of the model fit to GLODAPv2 observations of each steady-state tracer field used in the model optimization. For the constant, temperature-dependent, phosphate-dependent, and cellular growth model parameterizations of $R_{C:P}$, the model fit to observed DIC yielded R^2 values of 0.9130, 0.9090, 0.9108, and 0.9162, respectively. The same models fit to observed alkalinity yielded R^2 values of 0.8675, 0.8665, 0.8658, and 0.8670. DOC is given less weight than DIC and Alkalinity in the optimization. R^2 values for the modeled DOC fit to observations were 0.305, 0.3893, 0.5374, and 0.5272 for the constant, temperature-dependent, phosphate-dependent, and cellular growth model parameterizations of $R_{C:P}$, respectively.

temperature uniformly by about 3°C. This is consistent with the projected global mean sea surface temperature increase by 2100 projected under RCP8.5 (CMIP5 models) and SSP5-8.5 (CMIP6) (Kwiatkowski et al., 2020). In this sensitivity experiment, only the $R_{C:P}$ function is affected by the future conditions. We therefore can attribute all changes to the resulting carbon cycle equilibrium state to the effect of stoichiometric plasticity.

In the preindustrial steady-state optimization, we held the atmospheric pCO_2 fixed at a value of 278 ppm. When considering future change, it no longer makes sense to hold the atmospheric CO_2 concentration fixed. Instead, we added a prognostic equation for atmospheric pCO_2 in the form of a simple one-box model (Fu & Wang, 2022). This allows us to use the conservation of total carbon to determine how carbon is partitioned between the atmosphere and oceanic reservoirs as a function of the perturbed $R_{C:P}$ fields.

To isolate the impact of the $R_{C:P}$ parameterization on the carbon cycle, we make a number of simplifying assumptions: (a) We assume that the biological production of organic phosphorus remains fixed at the optimized model levels. The imposed nutrient decline affects only the $R_{C:P}$ parameterization, leaving the rest of the biogeochemical model unaffected. Because productivity is modeled using the biological uptake of DIP, a decrease in surface phosphate would otherwise reduce the total productivity of the system. For all experiments, we prescribe the biological uptake of DIP to that of the model optimized to modern climatology. (b) We ignore changes in air-sea gas exchange due to sea surface warming and salinity changes under the future scenario. The temperature and salinity inputs to the air-sea gas exchange equation are held fixed at the climatological values used in the model optimization. (c) In the cellular growth model, the input light field is also held fixed at climatological values. (d) We do not consider the impacts of changing large-scale circulation patterns. We use the same steady-state OCIM circulation pattern throughout all experiments. (e) Finally, it is important to note that our models are not time-evolving models. We only solve for the equilibrium state carbon cycle given a perturbed map of $R_{C:P}$ without computing the transient approach to the new equilibrium. Given the number of simplifying assumptions here, these model results should not be interpreted as accurate predictions of future ocean conditions. Instead, our perturbation experiments are intended to highlight the disparity in the magnitude and direction of change between the models optimized with different parameterizations of $R_{C:P}$.

3. Results

In this section, we will describe our results pertaining to the model optimization, the preindustrial steady-state tracer distributions, and the future sensitivity experiment. First, we show that all optimized models were able to reproduce the observed hydrographic tracer distributions well. We next discuss the spatial patterns of carbon-to-phosphorus uptake ratios, $R_{C:P}$, for each parameterization. We additionally examine the C:P ratios for the exported organic matter and the implied organic carbon export flux. Finally, we present the results of the idealized sensitivity experiment to demonstrate how different parameterizations of $R_{C:P}$ influence the partitioning of carbon dioxide between the atmosphere and ocean under perturbations to surface temperature and nutrient concentrations associated with climate change.

3.1. Model Performance

All models are able to reproduce the observed hydrography reasonably well. Compared to the model with a globally uniform $R_{C:P}$, the temperature-dependent, phosphate-dependent, and cellular growth models improve the model fit to hydrography (i.e., reduced the objective function value) by 0.8%, 8.4%, and 10.3%, respectively. All models are conditioned on the same modeled phosphorus cycle, which is optimized independently and captures more than 92% of the variance seen in the GLODAPv2 climatological DIP observations ($R^2 = 0.9281$). Figure 1 demonstrates the similar ability of each model to reproduce observed hydrographic tracer distributions of DIC, Alkalinity, and DOC. All models have a similar performance at matching the observed DIC and alkalinity fields,

Table 3
Optimized Parameter Values

Symbol				Value
b_P				$1.104 \pm 0.2\%$
k_{dP}				$1.65 \times 10^{-8} \pm 0.9\%$
α				$5.41 \times 10^{-7} \pm^{11\%}_{10\%}$
β				$0.23 \pm 4\%$
Symbol	Constant C:P	T-dependent	P-dependent	Cellular growth
b_C	$0.942 \pm 0.3\%$	$0.912 \pm 0.3\%$	$0.926 \pm 0.3\%$	$0.957 \pm 0.3\%$
d	$5.01 \times 10^3 \pm 0.8\%$	$5.20 \times 10^3 \pm 0.8\%$	$5.12 \times 10^3 \pm 0.7\%$	$4.97 \times 10^3 \pm 0.7\%$
k_{dC}	$2.58 \times 10^{-8} \pm 1\%$	$2.39 \times 10^{-8} \pm 1\%$	$2.96 \times 10^{-8} \pm 0.9\%$	$2.90 \times 10^{-8} \pm 0.9\%$
R_{rain}	$3.51 \times 10^{-2} \pm 0.7\%$	$3.61 \times 10^{-2} \pm 0.6\%$	$3.36 \times 10^{-2} \pm 0.6\%$	$3.33 \times 10^{-2} \pm 0.6\%$
$r^{\text{const}}_{C:P}$	$104.0 \pm 0.7\%$	–	–	–
c_1	–	–	$9.20 \times 10^{-3} \pm 1\%$	–
c_2	–	–	$4.81 \times 10^{-3} \pm 1\%$	–
c_3	–	$-1.01 \times 10^{-4} \pm 3\%$	–	–
c_4	–	$1.19 \times 10^{-2} \pm 1\%$	–	–
Q^{photo}_{10}	–	–	–	$3.56 \pm 2\%$
f_{stor}	–	–	–	$7.40 \times 10^{-3} \pm 3\%$
k_{S,T_0}	–	–	–	$9.34 \times 10^{-2} \pm^{6\%}_{5\%}$
r^{stor}_0	–	–	–	$2.15 \pm^{11\%}_{10\%}$
α_S	–	–	–	$0.39 \pm^{43\%}_{30\%}$

Note. A brief description of the parameters and their units can be found in Table 2. The first section contains the four phosphorus cycle parameters. These parameters are optimized using inorganic phosphorus observations, then held fixed for all carbon cycle configurations. The next section contains the four carbon cycle parameters which are optimized for each model configuration, regardless of the parameterization of $R_{C:P}$. The final section of the table shows the parameter values directly controlling the spatial pattern of $R_{C:P}$ in each model. The uncertainty values correspond to ±1 standard deviation of the posterior probability distribution function. For this calculation, we use Laplace's approximation to approximate the posterior pdf as a multivariate Gaussian distribution centered at the most probably parameter values.

with less than 2% difference in R^2 values for the model fit to observations of these fields. Partly because the DOC field is weighted less strongly in our objective function, the modeled DOC has larger discrepancies with the observations as well as larger differences between models. Parameterizations with strongly varying C:P ratios, namely the phosphate-dependent and cellular growth models, demonstrate superior performance in their representation of DOC compared to their less variable counterparts. Although the DOC misfit has only a modest impact on the objective function value, this improvement indicates that strongly varying C:P ratios are essential to accurately capture DOC:DOP gradients.

The optimal parameter values controlling $R_{C:P}$, listed in Table 3, are comparable to previous estimates described below. For the biogeochemical model in which we optimize a globally constant $R_{C:P}$ parameter, we find the global optimal $R_{C:P}$ value to be 104:1 molC:molP, which is close to the canonical Redfield value of 106:1 (Redfield, 1958) and to the value estimated from previous inverse model estimates, 105:1 (Teng et al., 2014). The parameterizations allowing for spatially variable $R_{C:P}$ also produce global mean values within 15% of the Redfield value of 106:1. However, the optimized empirical parameterizations of $R_{C:P}$ indicate a weaker temperature dependence and stronger phosphate dependence than reported in previous studies. For the temperature-dependent $R_{C:P}$ parameterization, the optimized slope and intercept parameters (Equation 2) are $c_3 = (-10.1 \pm 0.3) \times 10^{-5}$ molP(molC)$^{-1}$(°C)$^{-1}$ and $c_4 = (11.9 \pm 0.1) \times 10^{-3}$ molP(molC)$^{-1}$. The optimized slope corresponds to a weaker temperature dependence of $R_{C:P}$ than found in previous studies. For example, Yvon-Durocher et al. (2015) estimated that C:P ratios increases 2.6 fold from 0 to 30°C. In contrast, our temperature dependent $R_{C:P}$ model predicts that C:P ratios increase by just 36% over a similar temperature range. For the phosphate-dependent $R_{C:P}$ parameterization, the optimal slope and intercept parameter values (Equation 1) are $c_1 = 9.2 \pm 0.1$‰/μM and $c_2 = 4.81 \pm 0.05$‰. Our optimized intercept is consistent with previous estimates of

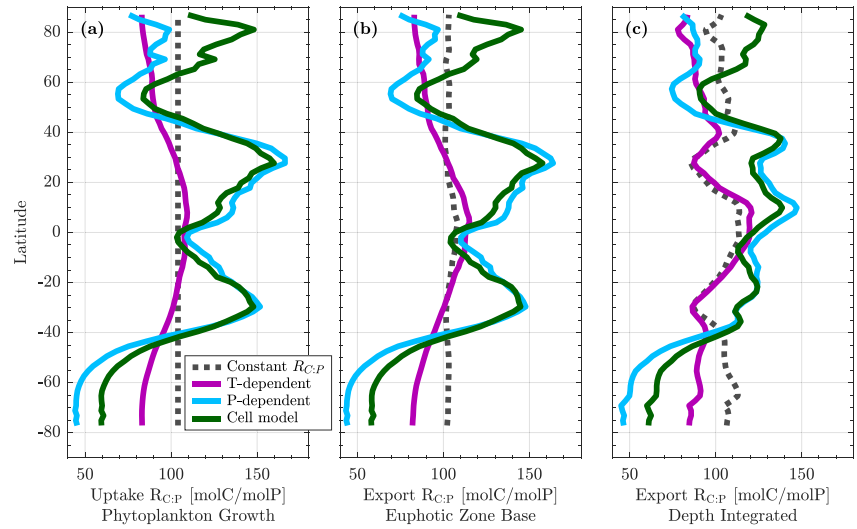

Figure 2. Comparison of zonal average C:P ratios between models optimized with each of the four $R_{C:P}$ parameterizations. Panel (a) illustrates the uptake C:P ratio of net community production. Panels (b) and (c) illustrate the C:P ratio of organic matter export computed using two methods, which differ in their sensitivity to lateral advection. The adjoint method (b) finds the C:P ratio of total organic matter export at the base of the model euphotic zone (approximately 73 m). The integrated DOM remineralization method (c) computes the ratio of water column integrated DOC and DOP remineralization beneath the euphotic zone. The zonal averages plotted in panels (a)–(c), are weighted by POP production, TOP export at the base of the euphotic zone, and deep water column total DOP remineralization, respectively. Because all models use the same phosphorus cycle model solution, these weights are equivalent across all four models.

$c_2 = 6.0 \pm 0.2‰$ and $4.8 \pm 0.5‰$ derived from linear regressions of P:C in suspended POM and $\left[PO_4^{3-}\right]$ using unbinned and binned-lognormal mean data sets (Galbraith & Martiny, 2015), as well as $c_2 = 5.3 \pm 1.0‰$ estimated by a separate inverse model optimization (Kwon, Holzer, et al., 2022). However, our optimized slope is larger than previous estimates of $c_1 = 6.9 \pm 0.4‰/\mu M$ and $c_1 = 7.3 \pm 0.6‰/\mu M$ (Galbraith & Martiny, 2015), and $c_1 = 6.6 \pm 1.8‰/\mu M$ (Kwon, Holzer, et al., 2022), indicating that our phosphate-dependent model has a stronger dependence on phosphate than other estimates. The stronger phosphate dependence of our model compared to that of Kwon, Holzer, et al. (2022) may result from the relative inflexibility of other components of the model that alter the $R_{C:P}$ of exported organic matter in our model. For example, our model does not allow for spatial variability in the remineralization rates of organic carbon and phosphorus. Thus, the exact parameter values are sensitive to the biogeochemical model configuration and should be re-optimized for any alterations of the biogeochemical model.

The optimized parameter values in the cellular growth model deviate from previous cellular models. Our f_{stor}, $Q_{10,\text{photo}}$, and α_S parameters are larger than analogous values used in previous cellular models (C. A. Garcia et al., 2020; Moreno et al., 2018; Shuter, 1979; Toseland et al., 2013), while our reference specific synthesis rate, k_{S,T_0}, is smaller than the assumed value of 0.168 hr^{-1} at 25°C used in the models of Shuter (1979) and Moreno et al. (2018). The deviations in parameter values will be discussed in Section 4.1.

3.2. Steady-State Tracer Distributions

3.2.1. $R_{C:P}$ of Organic Matter Production and Export

The production-weighted global mean $R_{C:P}$ of organic matter uptake varies by up to 25% between models, with even larger regional discrepancies (Figure 2a). The global mean uptake $R_{C:P}$ ranges from 99.0 for the temperature-dependent model to 123.9 for the phosphate-dependent model, with the constant model and cellular growth model producing intermediate mean values of 104.0 and 121.7, respectively. Figure 2a highlights the markedly different latitudinal gradients that emerge from each of the $R_{C:P}$ models. The phosphate-dependent model produces the largest range of $R_{C:P}$ values, with zonal averages reaching up to 175 in the Northern Hemisphere subtropics, and down to about 50 in the Southern Ocean. The temperature-dependent model produces the smallest range of values, with zonally averaged $R_{C:P}$ peaking at about 110 near the equator and gradually declining with latitude to a

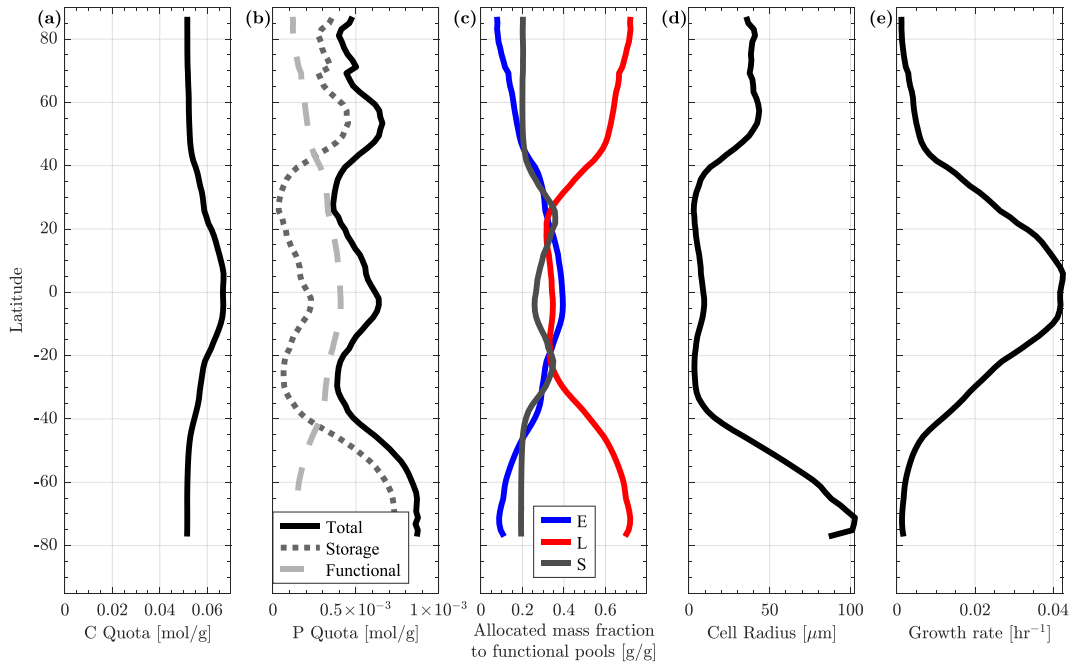

Figure 3. Zonal average growth strategy as a function of latitude produced by the cellular growth model optimized for the preindustrial steady-state. (a) and (b) illustrate the latitudinal gradients of the specific cellular carbon quota (a) and phosphorus quota (b). In (b), the phosphorus quota is further broken down to separate the contribution of non-essential phosphorus storage (dotted line) from the functional, non-storage component (dashed line) of the total cellular phosphorus quota. The solid line represents the total phosphorus quota and is the sum of the storage and functional components. In this model, $R_{C:P}$ is computed as the molar ratio of carbon and phosphorus quotas. The functional quotas are determined by the optimal growth strategy as a function of the environment, but independent of any non-essential luxury phosphorus storage. (c–e) illustrate the optimal cellular growth strategy, including (c) the investment in each functional apparatus, where $E + L + S = 1$. E represents the biosynthetic apparatus, L represents the photosynthetic apparatus, and S represents cell structure, including both size-independent (e.g., DNA) and surface-associated (e.g., cell membrane and nutrient uptake apparatus) structural components, (d) the cell radius and (e) the cellular growth rate. All zonal averages are weighted by volume of the model grid cell.

minimum value of 84 near the poles. The two empirical models are in good agreement on $R_{C:P}$ uptake near the equator and at high latitudes in the northern hemisphere. However, they diverge substantially in the subtropics and Southern Ocean. The phosphate-dependent model predicts much higher $R_{C:P}$ values in the subtropics and much lower $R_{C:P}$ values in the Southern Ocean than the temperature-dependent model. The cellular growth model follows a similar latitudinal trend to the phosphate-dependent model, with the highest values in the subtropics, and lowest values in the Southern Ocean. The latitudinal trends in $R_{C:P}$ found by the phosphate-dependent and cellular growth models are broadly consistent with the trends seen in ship-based POM measurements (Tanioka, Garcia, et al., 2022; Tanioka, Larkin, et al., 2022). Similar to these $R_{C:P}$ models, the C:P ratios measured in suspended POM are generally high in the subtropics, lower at high latitudes, and intermediate in equatorial regions. The phosphate-dependent and cellular growth models also capture the observed elevation of the subtropical peak in C:P stoichiometry in the Northern Hemisphere relative to the Southern Hemisphere (Tanioka, Garcia, et al., 2022). The cellular growth model better aligns with arctic POM observations, which indicate moderately elevated $R_{C:P}$ (Tanioka, Larkin, et al., 2022), whereas both empirical models predict relatively low $R_{C:P}$ in this region.

These latitudinal gradients in $R_{C:P}$ are driven by large-scale environmental variations. While the empirical functions are influenced by a single environmental factor, the cellular growth model reveals multiple mechanisms contributing to the latitudinal gradient of $R_{C:P}$ stoichiometry. Figures 3a and 3b illustrate the latitudinal gradients of the cellular carbon and phosphorus quotas individually. Figure 3b separates the contribution of non-essential phosphorus storage to the total phosphorus quota from the essential (non-storage) contribution to the quota. The cellular carbon quota and the non-storage fraction of the phosphorus quota both scale with the optimal cellular growth rate, with higher values at low latitudes, where warmer temperatures allow for faster synthesis rates

(Figures 3a, 3b, and 3e). In contrast, the luxury phosphorus storage pool—which is a function of phosphate availability and cell size—is independent of growth rate. The phosphorus storage pool therefore decouples the C:P stoichiometry from the cellular growth rate. These figures demonstrate qualitatively that the spatial structure of $R_{C:P}$ from this model is driven in large part by the variability in the luxury phosphorus storage term in the model. The strong phosphate dependence of the non-essential phosphorus storage (driven by an elevated f_{stor} value) emerges from the inverse model optimization. This result suggests that cells must store significant amounts of excess phosphorus in order for the growth model to produce $R_{C:P}$ patterns that are consistent with hydrographic observations.

Alongside the $R_{C:P}$ patterns, the cellular growth model identifies biogeographies of cellular investment in different functions across environmental gradients. Figure 3c illustrates the zonal average investment in each functional apparatus across latitudes. In subtropical gyres, high $R_{C:P}$ values can be attributed to an increased investment in surface-associated structures, including nutrient uptake machinery, and an accompanying reduction in the phosphorus rich biosynthetic apparatus. This restructuring is necessitated by the low nutrient concentrations in these regions, which limit the diffusive uptake rates of phosphorus and nitrogen. To effectively balance nutrient uptake, photosynthetic, and biosynthetic rates, cells adjust their resource allocation to prioritize nutrient uptake machinery. Given that nutrient uptake occurs at the cell surface, this adaptation involves reducing cell size (as depicted in Figure 3d). This reallocation reduces the cellular investment in biosynthetic and photosynthetic machinery, leading to a lower intracellular phosphorus content and, consequently, a higher C:P ratio. Conversely, at middle to high latitudes (greater than approximately 45°), abundant nutrients and larger cell sizes make the surface-associated structure pool, which scales with the surface area of the cell, insignificant relative to the total cell volume, resulting in a consistent allocation to cell structure (S) equal to the size-independent structural allocation (γ_S). Therefore, the latitudinal trend in cell strategy in these regions arises from the trade-off between photosynthesis and biosynthesis. Colder temperatures and lower light levels at high latitudes drive a more rapid decline in photosynthetic efficiency (α_I) than biosynthetic efficiency (k_{ST}), resulting in larger investments in photosynthesis (L) and less in biosynthesis (E) towards higher latitudes. Despite similar relative investments in the E, L, and S functional pools at high latitudes in both hemispheres, the $R_{C:P}$ values in the Northern and Southern Hemispheres have contrasting trends, with relatively high $R_{C:P}$ values in the Arctic and low $R_{C:P}$ values in the Southern Ocean. This discrepancy in $R_{C:P}$ values between the northern and southern high latitudes can be attributed to intracellular "non-essential" phosphorus storage, as illustrated by elevated phosphorus storage quotas in the Southern Hemisphere (Figure 3b). The Southern Ocean has higher observed nutrient concentrations than the Arctic Ocean, which consequently allows for larger cell sizes by increasing the diffusive nutrient flux. Thus, low $R_{C:P}$ values in the Southern Ocean are driven by high concentrations of intracellular phosphorus storage.

While our $R_{C:P}$ functions explicitly calculate the ratio of C:P taken up by phytoplankton in the surface ocean, it is the stoichiometry of exported material that ultimately controls the steady-state carbon reservoirs. The export $R_{C:P}$ is modulated by independent remineralization rates of carbon and phosphorus. Because all optimized models produced faster solubilization of POP relative to POC ($b_P > b_C$), the ratio of C:P in the particle export flux increases with depth. This is consistent with observational evidence that sinking organic particles become increasingly phosphorus depleted with depth (Tanioka et al., 2021). This mechanism allows for a more efficient biological pump, by allowing the same phosphorus atoms to fuel several cycles of production before being sequestered in the deep ocean.

Furthermore, export stoichiometric ratios include both the particulate and dissolved export fluxes, and thus are strongly influenced by the advection of dissolved organic matter. To account for this advection, we use the adjoint of the tracer transport equation to trace the remineralization flux of organic carbon and phosphorus back to where the organic matter last crossed the base of the euphotic zone (see Primeau et al., 2013). An alternative approach is to average the remineralization rate of organic carbon and phosphorus within a given water column. Because organic matter can be transported laterally and because organic phosphorus and organic carbon are not remineralized at the same rate, the two accounting methods yield different regional patterns even though they yield equivalent global averages.

The zonally averaged $R_{C:P}$ of organic matter export using each method is shown in Figure 2b (adjoint), and Figure 2c (water column remineralization). The adjoint method curve yields the average $R_{C:P}$ of the organic material as it is exported through the base of the euphotic zone. The resulting $R_{C:P}$ is nearly equal to the $R_{C:P}$ of net community production, with differences between the zonal average export $R_{C:P}$ and production $R_{C:P}$ remaining

well below 5%. The small difference is due to the lateral transport of DOM before it is exported through the base of the euphotic layer. The similarity suggests that the stoichiometry measured in surface POM samples is likely to be a good measure of the export $R_{C:P}$ as diagnosed using the adjoint method. The water column remineralization method, on the other hand, is strongly influenced by lateral advection and reveals that export fluxes at depth are decoupled from the surface production within a given water column.

The two methods show the largest differences in the subtropics. This is consistent with previous studies suggesting that roughly half of the DOC respired in the subtropical gyres originated elsewhere (Letscher & Moore, 2017). Because a significant portion of the organic material remineralizing in the gyres is advected in from higher latitudes, where production $R_{C:P}$ is generally low, the average export $R_{C:P}$ observed below the gyres is much lower than the average $R_{C:P}$ of organic matter production in this region. The difference between the two methods of determining the stoichiometry of exported organic matter suggests that accounting for DOM advection is critical to interpreting field measurements of export, as field methods measuring $R_{C:P}$ in sinking particulate matter might not reflect the stoichiometric ratios of total organic matter export.

3.2.2. Carbon Export

Our models show that the choice of $R_{C:P}$ parameterization has a notable effect on the magnitude of globally integrated carbon export fluxes. While all models are formulated using the same steady-state phosphorus cycle and therefore have equivalent total organic phosphorus (TOP) export, the integrated total organic carbon (TOC) export flux differs by up to 10% (1.3 Pg C yr^{-1}) between models. These differences occur despite nearly equivalent fits to the hydrographic data. The models with spatially variable $R_{C:P}$ result in steady-state estimates of TOC export that differ by up to 6% from the integrated TOC export flux of 14.1 Pg C yr^{-1} derived from assuming a globally constant $R_{C:P}$ value. The temperature-dependent, phosphate-dependent, and cellular growth models yield global TOC export fluxes of 13.3, 14.0, and 14.6 Pg C yr^{-1}, respectively. Thus, the baseline carbon export flux at steady state is sensitive to the representation of $R_{C:P}$.

The largest component of organic carbon export is the sinking particle flux, which consistently accounts for approximately 75% of the globally integrated TOC export flux, regardless of the $R_{C:P}$ parameterization. However, the distinction between POC and DOC is ambiguous due to the simplified cycling between particulate and dissolved organic matter in our model framework. The global-constant, temperature-dependent, phosphate-dependent and cellular growth models of $R_{C:P}$ result in global POC export fluxes at the base of the euphotic zone of 10.5, 10.0, 10.7, and 11.0 Pg C yr^{-1}, respectively. These particulate flux values are similar to the inverse model estimate of 10.6 ± 0.1 Pg C yr^{-1} from Wang et al. (2023), but larger than other previous estimates using inverse models (9.1 ± 0.2 Pg C yr^{-1} (DeVries & Weber, 2017), 7.3 ± 0.5 Pg C yr^{-1} (Nowicki et al., 2022)) as well as a satellite based food web model (5.9 ± 1.2 Pg C yr^{-1} (Siegel et al., 2014)). While our models project higher export, the inverse modeling method ensures that our estimates remain consistent with hydrographic observations. Discrepancies with other studies may arise from varying export definitions, including differing export horizons and transport pathways that impact the residence time of exported carbon. Direct comparisons are complicated by the ambiguity in distinguishing export pathways in our model, along with potential compensatory mechanisms in the biogeochemical model. For example, our larger export fluxes may be compensated by shallower remineralization depths than found in other models. Therefore, inter-model comparison is highly dependent on the export horizon chosen. A detailed analysis of how our model differs from other studies is beyond the scope of this paper however, as our primary focus centers on contrasting models with variable stoichiometry and the baseline case relying on a globally constant $R_{C:P}$.

The different globally integrated export fluxes between models stem from variations in the spatial pattern of organic carbon production as well as differing carbon remineralization depths across models. The optimized models that produce the largest export fluxes at the base of the euphotic zone concurrently find larger optimal parameter values for the exponent of the POC flux attenuation profile, b_C (see Table 3), enabling shallower respiration depths and thus shorter sub-surface residence times of the regenerated inorganic carbon. This compensation allows for all models to reproduce observed vertical DIC gradients reasonably well, despite the wide range of global export fluxes across models.

While all models produce similar overall trends of TOC export, the exact pattern of export varies depending on the parameterization of $R_{C:P}$ used in the model optimization (Figure 4). Figure 4a compares the zonally integrated TOC export across all models. Irrespective of the $R_{C:P}$ parameterization, all models consistently depict elevated

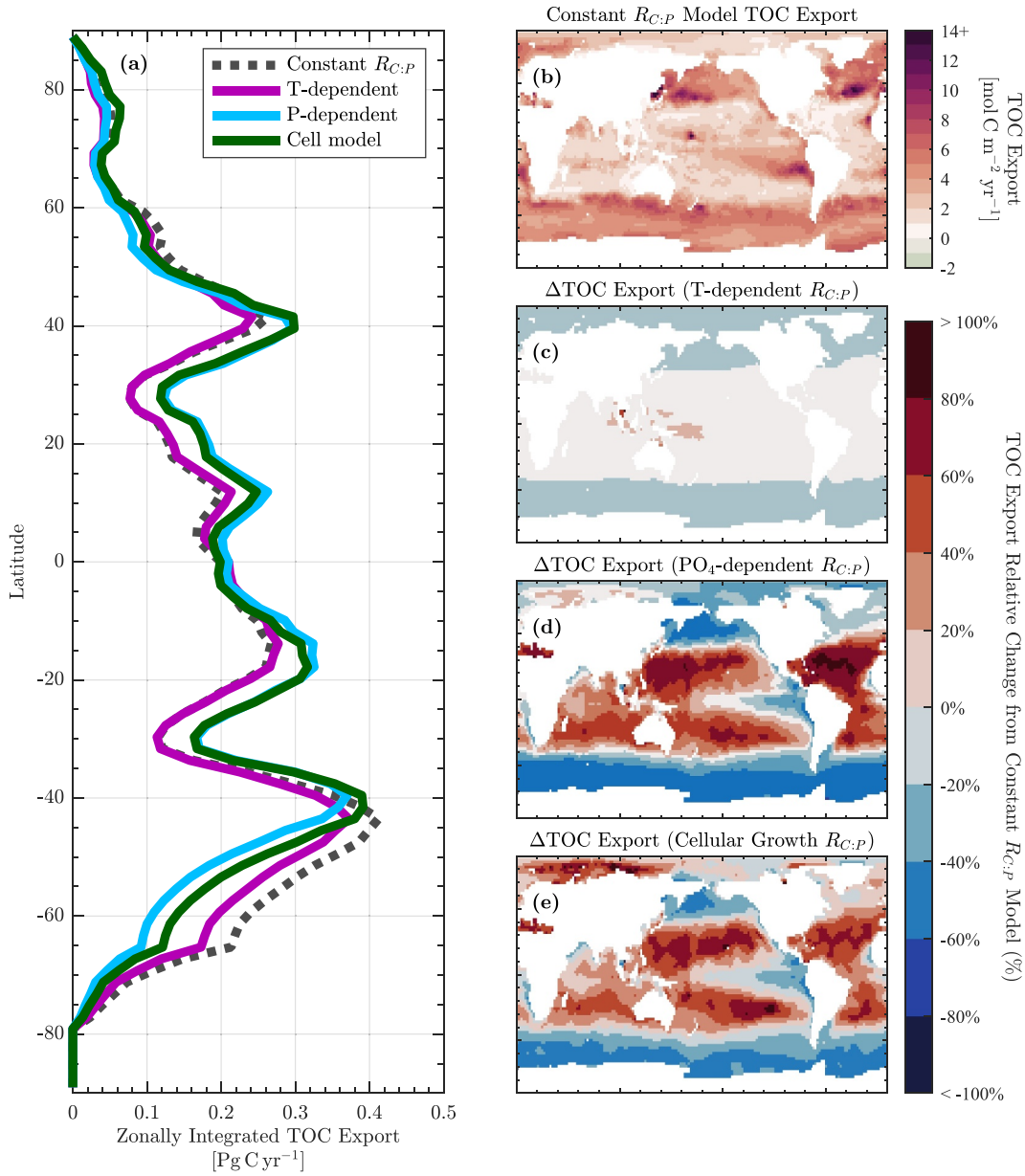

Figure 4. (a) Zonally integrated Total Organic Carbon export at the base of the euphotic zone for all models. (b) Spatial distribution of TOC export computed from the model using a global constant $R_{C:P}$. (c–e) Maps showing the TOC export anomaly from the constant $R_{C:P}$ case for each of the variable $R_{C:P}$ parameterizations.

export fluxes along the subtropical front of the Southern Ocean and in subpolar regions of the Northern Hemisphere, with relatively lower export fluxes in the subtropics. However, the adoption of different $R_{C:P}$ parameterizations introduces significant local and regional variations in the spatial distribution of carbon export. In comparison to the constant $R_{C:P}$ model, the three variable parameterizations yield increased TOC export in subtropical oceans and reduced export in the Southern Ocean (Figures 4b–4e). These deviations are relatively small for the temperature-dependent model, which finds export fluxes within 20% of the baseline model values across nearly the entire ocean. In contrast, the phosphate-dependent and cellular growth parameterizations result in over 50% higher export on average within subtropical gyres, with notable localized increases exceeding 80%, such as in the core of the North Atlantic subtropical gyre. There is also substantial discrepancy between models in the Arctic, where the cellular growth model finds significantly increased export over all other $R_{C:P}$

parameterizations. Thus, regional disparities among models can well surpass the up to 10% differences observed in globally integrated TOC export fluxes.

Many of the largest disagreements between models correspond to regions with the highest TOC export fluxes. In all models, the largest local TOC export fluxes occur in the mid-latitude North Atlantic (approximately 40–50°N), where there is high productivity as well as substantial downward transport, associated with the sinking branch of the meridional overturning circulation, in the model. Export in this region is further amplified when using the phosphate-dependent and cellular growth models compared to the baseline case with globally constant $R_{C:P}$. The phosphate-dependent model displays the greatest degree of deviation from the constant model, with TOC export fluxes up to 80% larger than the baseline model in the North Atlantic (Figure 4d). Zonally integrated TOC export fluxes peak along the subtropical front of the Southern Ocean (between 40 and 45°S) in all models. This region also marks a transition where the anomaly of each variable $R_{C:P}$ model from the baseline case switches sign, with the variable $R_{C:P}$ models estimating increased export toward the equator and decreased export to the south relative to the model with a globally constant $R_{C:P}$ (Figures 4c–4e). The constant stoichiometry model finds 3.7 Pg C yr^{-1} of TOC export integrated over the ocean region south of 45°S, constituting roughly 26% of the globally integrated TOC export flux. Models with variable stoichiometry reduce this regional export flux by 16%, 47%, and 33% using the temperature-dependent, phosphate-dependent, and cellular growth $R_{C:P}$ parameterizations, respectively. This region contributes a substantial fraction of the global carbon export. However, implementing parameterizations of $R_{C:P}$ with more spatial variability reduces the degree to which the Southern Ocean dominates the global carbon export flux. Therefore, narrowing down the range of possible C:P ratios in this region could greatly improve our confidence in global carbon export. Accurately modeling the stoichiometry of exported organic matter in the Southern Ocean will thus be essential to reducing uncertainty in global carbon export fluxes.

3.3. Sensitivity to Future Change

We next looked at the sensitivity of each model to future change by performing idealized sensitivity experiments in which we imposed a hypothetical future environmental conditions on the $R_{C:P}$ functions in each model. In these experiments, the global distribution of phytoplankton uptake $R_{C:P}$ is calculated using each optimized $R_{C:P}$ parameterization given uniformly warmer temperatures and decreased nutrient concentrations in the surface ocean. The $R_{C:P}$ functions are perturbed by imposing a 3°C temperature increase, a 31% phosphate decrease, and a 21% nitrate decrease globally, while all other model inputs are held fixed. The carbon cycle model responds to the perturbed $R_{C:P}$ by adjusting the distribution of carbon reservoirs to a new steady-state solution. From the new model solution, we can calculate the change in export fluxes and stoichiometry.

The imposed surface temperature increase and phosphate decrease change the export $R_{C:P}$ pattern predicted by both empirical models as well as the cellular growth model, while the model with globally uniform $R_{C:P}$ remains unchanged. Figure 5a illustrates the change in zonal average export $R_{C:P}$ for each $R_{C:P}$ function when computed using the hypothetical future conditions relative to the preindustrial steady-state. For all models with an environmental dependence of $R_{C:P}$, the zonal average export $R_{C:P}$ increases everywhere, however the magnitude and spatial pattern of the change varies between models. The temperature-dependent model shows the weakest response to the imposed conditions. Given a uniform temperature increase of 3°C in the model euphotic zone, the temperature-dependent model produces 3% higher export $R_{C:P}$ values on average globally, relative to the preindustrial case. This change in export $R_{C:P}$ varies slightly with latitude, with regional increases ranging from less than 2.2 molC/molP at high latitudes to greater than 4.0 molC/molP near the equator. The response of the phosphate-dependent model to the perturbed surface phosphate field is more pronounced. Given a globally uniform 31% relative decline in euphotic zone phosphate concentration, the phosphate-dependent $R_{C:P}$ model predicts 18.5% higher export $R_{C:P}$ values on average than produced given preindustrial conditions. For this model, the zonal average change in export $R_{C:P}$ ranges from 9.3 to 18.7 molC/molP, with the smallest changes in the subtropical gyres, and the largest magnitude changes occurring along the subtropical front of the Southern Ocean and in the high latitude Northern Hemisphere (Figure 5a).

Unlike the empirical models, which respond to only a single environmental driver, the cellular growth model export $R_{C:P}$ is influenced by changes in both the perturbed temperature and nutrient fields. In the cellular growth model, the warmer temperatures and lower nutrient concentrations lead to a 16% increase in export $R_{C:P}$ on average globally. This model predicts a similar pattern of change in export $R_{C:P}$ as the phosphate-dependent model, with the smallest increases in the subtropics and largest increases in the Arctic, where export $R_{C:P}$

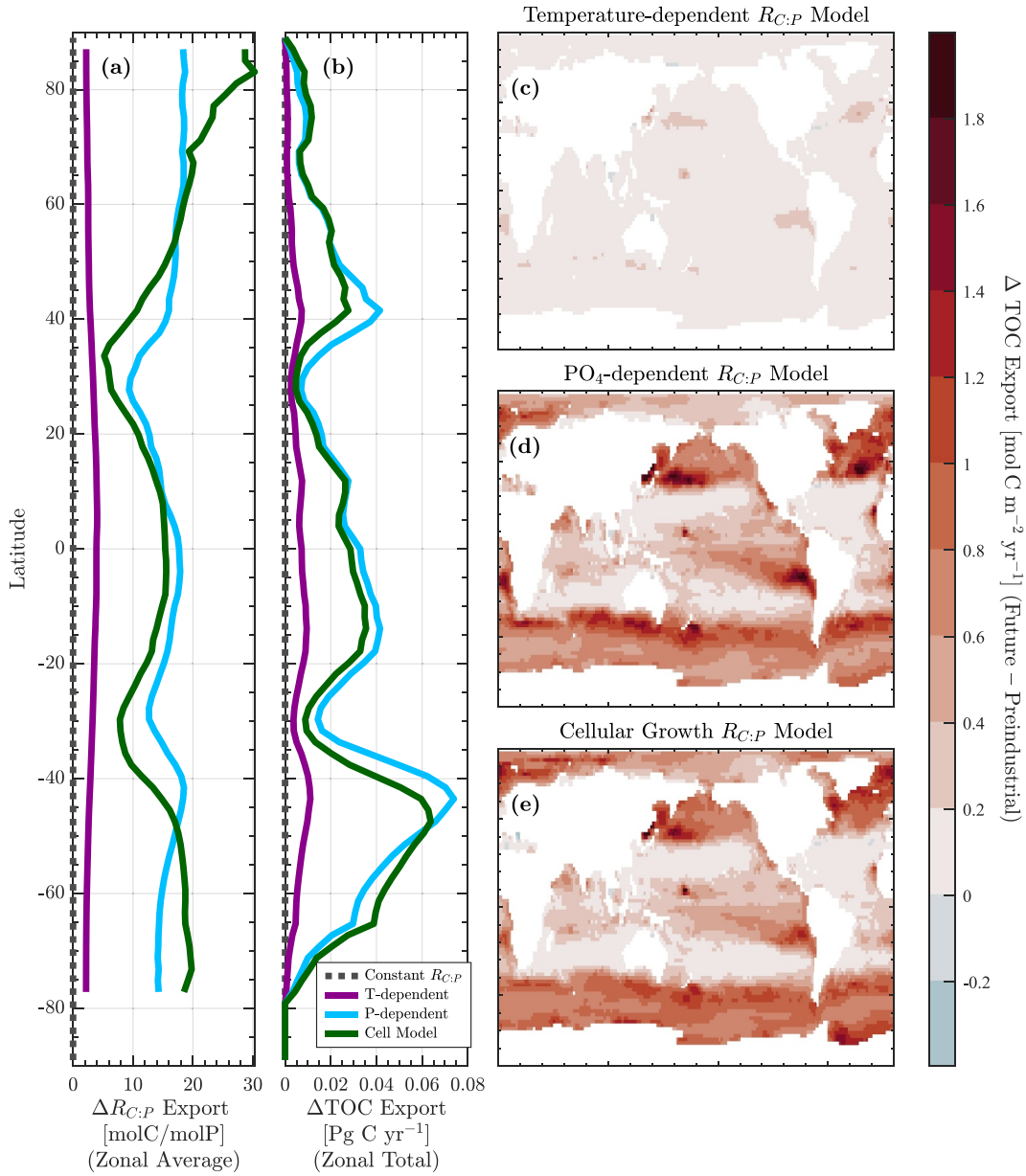

Figure 5. Predicted future change relative to the preindustrial state of (a) the zonal average export $R_{C:P}$ (weighted by total organic phosphorus export) and (b) zonally integrated total organic carbon (TOC) export at the base of the euphotic zone (73 m), calculated using the adjoint method. (c–e) Maps showing the projected change in TOC export from preindustrial steady state given a perturbed phytoplankton uptake $R_{C:P}$ pattern predicted by each variable $R_{C:P}$ parameterization. In this figure, the "future" scenario refers to the sensitivity experiment in which the model $R_{C:P}$ pattern is perturbed by a uniform increase in euphotic zone temperatures by approximately 3°C and reduction in euphotic zone DIP and DIN concentrations by 31% and 21%, respectively.

values increase by up to 30 molC/molP relative to preindustrial values. Additionally, the cellular growth model $R_{C:P}$ responds nonlinearly to temperature change. Given the uniform temperature increase alone, the cellular growth model predicts export $R_{C:P}$ increases at low latitudes and decreases at high latitudes (Figure S1). At high latitudes, the phosphate-dependence of $R_{C:P}$ is even stronger in the cellular growth model than using the linear phosphate-dependent model. The net effects of reduced surface nutrients and warmer temperatures in the arctic lead to larger increases in $R_{C:P}$ than seen with the phosphate-dependent model. This occurs even though the increased temperature acts to lower $R_{C:P}$ at high latitudes in the cellular growth model. These findings highlight

the complex interactions between temperature, nutrients, and phytoplankton stoichiometry, underscoring the importance of considering multiple environmental drivers when assessing changes in export $R_{C:P}$.

The perturbed $R_{C:P}$ patterns alter the steady-state total organic carbon (TOC) export flux in all models with environmentally dependent $R_{C:P}$ functions. All of the variable stoichiometry parameterizations lead to higher future carbon export than the model using a globally constant $R_{C:P}$ value, which predicts no change from the preindustrial steady state value of 14.1 Pg C yr^{-1}. When imposing warmer temperatures and reduced nutrient concentrations, the global TOC export increased by 0.4 Pg C yr^{-1} (3%) to 13.8 Pg C yr^{-1} for the temperature-dependent $R_{C:P}$ model, by 2.2 Pg C yr^{-1} (16%) to 16.2 Pg C yr^{-1} for the phosphate-dependent $R_{C:P}$ model, and by 2.0 Pg C yr^{-1} (13%) to 16.6 Pg C yr^{-1} for the cellular growth $R_{C:P}$ model. While future conditions push all models toward a regime with higher organic carbon export fluxes, the magnitude of the change is dependent on the model representation of $R_{C:P}$.

Furthermore, the choice of $R_{C:P}$ parameterization impacts the spatial pattern of the modeled change in TOC export in an altered climate. Figures 5b–5e illustrate the change in TOC export in the future sensitivity experiment relative to the preindustrial steady state. The phosphate-dependent model shows the largest magnitude changes in TOC export. In the Southern Ocean, the phosphate-dependent model predicts the greatest increase in TOC export along the subantarctic front (Figure 5d; near 45°S), where the greatest magnitude of zonally integrated TOC export occurs. In contrast, the cell model predicts that the amount of carbon export would increase more uniformly across the Southern Ocean than the phosphate-dependent model. The largest increases in zonally integrated carbon export occur at mid-latitudes (Figure 5b), where there is already high TOC export in the preindustrial steady state run (Figure 4a). The magnitude of this increase is smaller in the temperature-dependent model than the other two variable $R_{C:P}$ parameterizations. Thus, the choice of $R_{C:P}$ function significantly impacts model predictions of both the magnitude and spatial distribution of future carbon export.

In addition, the perturbed $R_{C:P}$ patterns drove a net decline in atmospheric pCO_2 in the future sensitivity experiments for all environmentally dependent $R_{C:P}$ models. In the future sensitivity experiments, we coupled a one-box atmosphere to the system, holding the total amount of carbon in the ocean-atmosphere system fixed to the total amount of carbon diagnosed from the solution of the preindustrial model. This allowed us to compute the change in atmospheric pCO_2 caused by the altered $R_{C:P}$ patterns. Forcing the temperature-dependent, phosphate-dependent and cellular growth $R_{C:P}$ functions with warmer temperatures and lower surface nutrient concentrations reduced atmospheric pCO_2 by 5, 24, and 21 ppm respectively, relative to the preindustrial steady state model solution. Thus, stoichiometric plasticity increases the biological uptake of atmospheric CO_2 under future conditions, and the strength of this effect depends on the assumed environmental drivers of $R_{C:P}$.

4. Discussion

4.1. Constraining the Cellular Growth Model Parameters

Our inverse modeling approach provides a valuable framework to evaluate the consistency of detailed mechanistic cellular-level models with geochemical constraints provided by hydrographic data, bridging the gap between understanding microbial functioning and global biogeochemistry. By utilizing climatological hydrographic tracer observations, our optimization captures long-term average export fluxes of phosphorus and carbon. Accurate representation of these fluxes is crucial for understanding carbon storage in the deep ocean and nutrient dynamics within the euphotic zone. Furthermore, the balance between carbon export and ventilation rates plays a critical role in setting atmospheric CO_2 concentrations, with shifts in this balance potentially explaining glacial-interglacial fluctuations in atmospheric pCO_2 (Sigman & Boyle, 2000). While previous studies have used inversion techniques to tune parameter values based on suspended particulate organic matter (POM) observations (e.g., C. A. Garcia et al., 2020), our novel approach uses only the model fit to global hydrographic data to constrain parameters within the cellular scale growth model. This allows us to avoid potential biases due to limited coverage of in situ stoichiometric observations, and accounts for the possibility of decoupled organic carbon and phosphorus degradation pathways. This method also demonstrates a novel way of constraining globally representative parameter values controlling cellular physiology. A major challenge of applying mechanistic biological models at the global scale is how to represent globally relevant characteristics of a highly diverse community. Using the hydrography to optimize the parameter values in the cell model allows us to obtain physiological parameter values representative of the community as a whole. Model parameters describing physiological rates are often set using rates measured in culture experiments. Lab-based estimates of

physiological rates typically come from a single species, rather than a community average. The bulk community response to environmental change is controlled by complex ecosystem interactions, which are difficult to recreate in laboratory settings. This includes both acclimation and shifts in community composition. Since the community response may be fundamentally different than the response of an individual species, using experimentally derived values could lead to inaccuracies in the model output (Franks, 2009; Hagstrom & Levin, 2017). Therefore, using global hydrographic data provides a valuable alternative to better understand and constrain parameter values in the cellular growth model.

However, unexpected optimal values suggest that we need to reevaluate the cellular mechanisms represented in the model. The optimization of our mechanistic model of phytoplankton growth yielded unexpectedly large parameter values, particularly for parameters affecting the temperature dependence of phytoplankton growth and the amount of luxury nutrient storage in cells. In our optimized cellular growth model, we found that the parameter controlling the temperature dependence of photosynthesis, Q_{10}^{photo}, had an unrealistically large value of 3.56. This is significantly higher than previous estimates of the Q_{10} of photosynthesis, which have ranged from 1.0 to 2.19 (Raven & Geider, 1988). This finding holds intriguing implications for understanding how temperature regulates cellular functioning and elemental composition on a global scale. Our high Q_{10}^{photo} value leads to an inverse relationship between temperature and $R_{C:P}$ at high latitudes, where growth rates are low. This contradicts a recent observational study by Tanioka, Garcia, et al. (2022), which found a strong positive correlation between temperature and $R_{C:P}$ of suspended POM at high latitudes, as well as the translation-compensation hypothesis, which predicts that $R_{C:P}$ increases with temperature due to enhanced efficiency of biosynthetic enzymes and therefore reduced requirement for phosphorus-rich ribosomes (Moreno & Martiny, 2018). Consequently, our model may be missing a key mechanism of cellular growth. Tanioka, Garcia, et al. (2022) found that the relationship between temperature and $R_{C:P}$ predicted by translation compensation is only observed in cold waters, suggesting that an alternate mechanism may dominate in warm waters. Including a corresponding mechanism to the cellular growth model could enable a more realistic Q_{10}^{photo} value.

The similarity between the $R_{C:P}$ patterns simulated by the phosphate-dependent and cellular growth models arises from the strong influence of phosphate concentration on the phosphorus storage pool in the cell model. The parameter optimization yields a very strong dependence of the total cellular phosphorus quota on phosphate availability. This is achieved by increasing the value of the scaling parameter, f_{stor}, on the luxury phosphorus storage equation, which sets the extent to which the intracellular phosphorus storage pool contributes to the total phosphorus quota of the cell. The optimal value allows intracellular inorganic phosphorus storage to account for up to 90% of the total phosphorus quota of the cell. Since the magnitude of the storage pool is a function of phosphate concentration in the water, this means that the total phosphorus quota of the cell has a much stronger nutrient dependence than the carbon quota of the cell. Thus, phosphate availability exerts a strong control on $R_{C:P}$ in the optimized cellular growth model. Evidence of very large allocations to intracellular phosphorus storage has been found in laboratory and field studies. Over 80% of the P quota in diatoms (Liefer et al., 2019) and up to 25% of the P quota in *Trichodesmium* in the phosphate depleted oligotrophic Sargasso Sea (Orchard et al., 2010) has been attributed to intracellular inorganic phosphorus storage. In contrast, a previous study by C. A. Garcia et al. (2020), which optimized a similar cellular growth model to in situ observations of $R_{C:P}$ in suspended POM, found optimal parameter values indicating that luxury phosphorus storage had only a minor effect on C:P ratios. This disparity highlights that the role of luxury storage is still highly uncertain. Because luxury phosphorus storage may be a major driver of global patterns of $R_{C:P}$, future work should focus on developing a more mechanistic understanding of phosphorus storage and improving the model representation of this pool.

The heavy reliance on phosphorus storage suggests that the mechanistic trade-offs between functional macromolecules needed for growth may not be enough to capture the stoichiometry of exported organic material. The strong influence of luxury storage may result from missing export processes in our biogeochemical model. It is possible that the bulk export signal is influenced by detritus which has been reprocessed through the food web, leading to bulk POM stoichiometry that differs from that of phytoplankton. The predicted cell model parameters could also result from errors in our biogeochemical model. For example, the parameters could be pushed to unrealistic values in order to compensate for errors in the model POP productivity field. In our model, organic carbon production is the product of the modeled POP production and uptake $R_{C:P}$. Errors in the spatial pattern of POP production could be introduced by errors in the satellite-derived spatial pattern of NPP or by errors in the model DIP field at the surface. The modeled DIP concentrations may be biased at the surface because the surface

layer is highly dynamic and constitutes a relatively small volume of the global ocean. Another missing process in our biogeochemical model that could affect the parameters controlling uptake $R_{C:P}$ is spatially variable remineralization rates of organic carbon and phosphorus. Sediment trap observations suggest that remineralization rates are temperature dependent (Marsay et al., 2015). However, our model assumes that remineralization rates are constant globally. This could introduce biases in the optimal $R_{C:P}$ pattern as the uptake $R_{C:P}$ pattern must compensate for the lack of variability in remineralization rates in order to reproduce the hydrographic DIC observations. Additionally, unrealistic parameter values could stem from incorrect assumptions regarding non-optimized parameters in the cell model, as we only optimized a subset of parameters that we expected to have the strongest influence on $R_{C:P}$.

Despite these limitations, the cellular growth model offers a promising avenue for further investigation. The results of the optimization provide insights into areas that warrant future observational efforts. For instance, the cellular growth model suggests that cells must store significant amounts of excess phosphorus to produce $R_{C:P}$ patterns that are consistent with hydrographic observations. However, the understanding of inorganic phosphorus (e.g., polyphosphate) storage in the open ocean remains limited. Therefore, future observations are crucial to assess whether variations in polyphosphate storage represent a major driver of global patterns of phytoplankton stoichiometry. Additionally, the cell model could be improved by incorporating other data sources. Notably, the cell model produces more than just $R_{C:P}$; the optimal cell strategy is also characterized by cell size and growth rate. By imposing constraints on these traits from in situ data or satellite remote sensing, we may obtain a more robust optimal parameter set.

4.2. Optimized Model Performance

Of the four $R_{C:P}$ parameterizations we implemented, the cellular growth model best reproduces hydrographic observations. However, the similar fit of the phosphate-dependent model suggests that phosphate is a dominant control on phytoplankton $R_{C:P}$ stoichiometry at the global scale. The cellular growth model can help us understand the mechanisms driving the $R_{C:P}$ patterns. In particular, the strong phosphate dependence of $R_{C:P}$ can be attributed primarily to intracellular inorganic phosphorus storage in our cellular growth model.

All models are able to provide a good fit to the hydrography, with only small improvements in the R^2 fit values depending on the choice of $R_{C:P}$ parameterization. This is because the impact of $R_{C:P}$ on deep ocean inorganic carbon pools is relatively small compared to other factors such as the impact of the physical circulation on the carbon solubility pump. While all models produce good fits to the hydrographic observations overall, the vast quantity of observations used in calculating the objective function means that the small differences in the model-data misfit are statistically significant. Comparing the different models is not straightforward due to the differing numbers of adjustable parameters and due to differences in the flexibility of the different model architectures in shaping patterns of $R_{C:P}$. Although the cell model was able to slightly improve the fit to observations compared to the phosphate-dependent parameterization, it had a larger number of adjustable parameters. Because of the many caveats and simplifications in our model, we chose not to pursue a formal statistical analysis between these models. Instead, the purpose of this analysis is to demonstrate how the cellular growth model provides a more mechanistic understanding of the emergent $R_{C:P}$ patterns than empirical models.

It is important to note that the ability of each model to fit the observations is dependent on the model representation of other processes that interact with the modeled $R_{C:P}$ to affect the model fit to the hydrography. For example, export $R_{C:P}$ is controlled by the interacting effects of variable $R_{C:P}$ of phytoplankton uptake and remineralization. Our simple parameterization of remineralization may not accurately represent the temperature dependence of phosphorus or carbon remineralization. This could impact the pattern of export $R_{C:P}$, which affects the model fit to deep ocean DIC. However, the close similarity between uptake $R_{C:P}$ and export $R_{C:P}$ values at the base of the euphotic zone seen in Figure 2 implies that within the euphotic zone of our model, remineralization plays a relatively minor role in modulating export stoichiometry. Therefore, the potential impact of spatially variable remineralization rates for organic phosphorus and carbon may be limited in our model.

4.3. Implications for Future Biological Carbon Pump

Most climate models predict that organic carbon export will decline in the future. The projected response of the global POC export flux to climate change varies widely across 19 CMIP6 earth system models, with estimates ranging from −41% to +1.8% change by 2100 from preindustrial, under the high emissions Shared

Socioeconomic Pathway SSP5-8.5 scenario (Henson et al., 2022). This decline in biological carbon export is generally attributed to surface warming leading to increased stratification and reduced nutrient supply to the surface ocean, thus increasing nutrient limitation and reducing the amount of net primary production that can be supported in the euphotic zone. Previous studies have suggested that changes to phytoplankton physiology could buffer the expected decline in ocean NPP (Tanioka & Matsumoto, 2017). The magnitude of this buffering effect is highly uncertain, with some claims that it could entirely offset the decline in NPP due to a decline in nutrient supply to the surface ocean (Kwon, Sreeush, et al., 2022). In our model, the magnitude of this buffering effect is sensitive to the choice of $R_{C:P}$ parameterization. The three models suggest changes in phytoplankton stoichiometry could offset a 3%–16% change in global carbon export (between 0.4 and 2.2 Pg C yr^{-1}) and draw down the global average atmospheric pCO_2 by between 5 and 24 ppm given a uniformly warmer and more nutrient limited surface ocean.

These increases in the biological uptake of atmospheric CO_2 are small in comparison to other anticipated perturbations to the biological carbon pump that were not considered in our future sensitivity experiments. For example, another sensitivity run of this model showed that an equivalent reduction in the phosphate concentration supplying POP production would cause an increase of roughly 55 ppm pCO_2, equivalent to a 31% reduction in TOC export, regardless of $R_{C:P}$ parameterization. This response is larger than the effect of changing $R_{C:P}$ on atmospheric pCO_2. Thus, $R_{C:P}$ plasticity cannot fully compensate for productivity declines due to reduced nutrient availability using any of the $R_{C:P}$ parameterizations presented here. Moreover, these responses are dwarfed by the projected changes in atmospheric pCO_2 due to anthropogenic emissions. Current emissions scenarios project pCO_2 values between 393 and 1,135 ppm by 2100 (i.e., up to >800 ppm higher than the preindustrial steady state atmospheric CO_2 concentration of 278 ppm) (Meinshausen et al., 2020). These results suggest that, in the absence of extreme carbon dioxide removal strategies, the potential future increase in phytoplankton $R_{C:P}$ may only have a minor influence on atmospheric pCO_2 in comparison to the rise due to anthropogenic emissions. Although, under negative emissions scenarios that adopt marine carbon dioxide removal strategies based on enhancing biological production (e.g., nutrient fertilization, artificial upwelling and downwelling, and seaweed cultivation (reviewed in National Academies of Sciences, Engineering, and Medicine (2022))), the effect of stoichiometric plasticity may become more significant. However, due to the idealized nature of our future sensitivity test—which does not take into account spatial patterns of environmental change—more sophisticated experiments within a coupled prognostic model framework would be needed to better assess the potential buffering effect of stoichiometric plasticity.

While stoichiometry is only one of many factors influencing the strength of the biological carbon pump, we find that the relative changes in ocean carbon export due to only a change in phytoplankton $R_{C:P}$ are of the same order of magnitude as projected changes in global carbon export by 2100. Therefore accounting for stoichiometric plasticity could significantly influence future projections of the biological carbon pump, and thus warrants further investigation. Future work should extend beyond the simple uniform change experiments performed here to look at the effects of $R_{C:P}$ functions within prognostic climate models. Embedding variable stoichiometry in more mechanistic earth system models would allow us to better synthesize the combined effects of stoichiometry, changing nutrient supplies, surface warming, and other ecosystem changes on biological carbon fluxes.

5. Conclusions

Our understanding of carbon export fluxes depends on an accurate representation of phytoplankton stoichiometry in global models. Despite nearly equivalent fits to the hydrographic data, models implementing different parameterizations for $R_{C:P}$ produced estimates of global total organic carbon export for the preindustrial steady state that differed by up to 10% (1.3 Pg C yr^{-1}), with even more substantial regional differences. The parameterization used to model $R_{C:P}$ also had a significant impact on the magnitude of the potential buffering effect of phytoplankton physiology on projected declines in export production. However, regardless of the parameterization chosen, the buffering effect was small compared to projected changes due to human activity. This indicates that the C:P compensation feedback loop is unlikely to completely compensate for declining primary production in the future.

To accurately assess carbon fluxes in the ocean, we need a more mechanistic understanding of what drives variability in phytoplankton stoichiometric ratios. While empirical models have been a powerful way to incorporate variable stoichiometry into global models at relatively low cost, these simple models lack causality needed to predict future change. Despite its limitations, the mechanistic model described here offers a way forward by

providing biological constraints on how phytoplankton physiology changes globally. Future work is needed to refine the processes represented in the cellular growth model.

Appendix A: Biogeochemical Model Equations

The three tracers in the phosphorus cycle model are dissolved inorganic phosphorus (DIP), dissolved organic phosphorus (DOP), and particulate organic phosphorus (POP). The governing equations for the phosphorus cycle are listed below.

$$\left[\frac{d}{dt}+\mathbf{T}\right][\mathrm{DIP}] = -\gamma[\mathrm{DIP}] + \kappa_{dP}[\mathrm{DOP}] + \kappa_g\left([\mathrm{DIP}] - \langle[\mathrm{DIP}]_{\mathrm{obs}}\rangle\right) \tag{A1}$$

$$\left[\frac{d}{dt}+\mathbf{T}\right][\mathrm{DOP}] = \kappa_p[\mathrm{POP}] - \kappa_{dP}[\mathrm{DOP}] \tag{A2}$$

$$\left[\frac{d}{dt}+\mathbf{S}_{\mathrm{POP}}\right][\mathrm{POP}] = \gamma[\mathrm{DIP}] - \kappa_p[\mathrm{POP}] \tag{A3}$$

In these equations $\mathbf{T}$ is the transport operator for tracers in the dissolved phase and $\mathbf{S}_{\mathrm{POP}}$ is the transport operator for tracers in the particulate phase. $\mathbf{T}$ is obtained from the data-constrained Ocean Circulation Inverse Model (OCIM2; DeVries & Holzer, 2019) is defined such that, for a tracer c,

$$\mathbf{T}c \equiv \nabla\cdot(\mathbf{u}c - \boldsymbol{\kappa}\nabla c), \tag{A4}$$

where $\mathbf{u}$ is the residual mean circulation and $\boldsymbol{\kappa}$ is the eddy-diffusion tensor. The $\mathbf{S}_{\mathrm{POP}}$ is defined such that

$$\mathbf{S}_{\mathrm{POP}}[\mathrm{POP}] \equiv \nabla\cdot(\mathbf{w}_{\mathrm{POP}}[\mathrm{POP}]), \tag{A5}$$

where $\mathbf{w}_{\mathrm{POC}}$ is the sinking velocity for POP. To obtain a vertical particle flux that attenuates following a power law function with depth, we parameterize the downward sinking speed of POM to increase linearly with depth using the expression, $w_{\mathrm{POC}}(z) = (\kappa_p/b_P)\,z$, where z is the vertical coordinate equal to zero at the sea surface and decreasing with depth, κ_p is a fixed particle dissolution rate constant, and b_P is the globally constant exponent of the power law function, $J(z) = J(z_0)\,(z/z_0)^{-b_P}$, with $J(z)$ and $J(z_0)$ representing the sinking fluxes at depths z and $z_0 = -73.4$ m, respectively.

The net production of POP ($J(z_0)$) is equivalent to the biological phosphate uptake in the model's euphotic zone, $z > z_0 = -73.4$ m. We assume that no photosynthesis occurs below $z = z_0$. The production of POP is parameterized to be proportional to the modeled DIP concentration with a spatially varying uptake rate constant, $\gamma(\mathbf{r})$, where $\mathbf{r}$ is the position coordinate. The rate constant is in turn parameterized in terms of a satellite-based estimate of net primary productivity (NPP) and surface DIP observations, following Teng et al. (2014) and Wang et al. (2023), and similar to Kwon, Holzer, et al. (2022),

$$\gamma(\mathbf{r}) = \begin{cases} \alpha\dfrac{\left[\frac{\mathrm{NPP}(\mathbf{r})}{\mathrm{NPP}_0}\right]^{\beta}}{\frac{[\mathrm{DIP}]_{\mathrm{obs}}(\mathbf{r})}{[\mathrm{DIP}]_0}}, & \text{if } z < z_0, \\ 0, & \text{otherwise.} \end{cases} \tag{A6}$$

NPP is estimated using the Carbon-based Productivity Model (Westberry et al., 2008) and has units of mmol C m^{-2} s^{-1}. $[\mathrm{DIP}]_{\mathrm{obs}}$ is the climatological mean DIP observations (H. E. Garcia et al., 2014), binned to our model grid, with units of mmol m^{-3}. The scaling factor α and exponent β are globally uniform parameters that are estimated as part of the inversion. α is in units of s^{-1} and β is dimensionless. This scaling characterizes the effect of the whole community on organic matter export production. α represents the net role of grazing pressure, trophic interactions and the microbial loop, converting nutrient uptake into productivity of the net community.

NPP_0 and $[DIP]_0$ are included to non-dimensionalize NPP and DIP and have values of 1 mmol C m^{-2} s^{-1} and 1 mmol m^{-3}, respectively. For simplicity, the depth-integrated NPP is split evenly between the two vertical layers in the model euphotic zone. We do not take into account vertical structure of primary productivity due to the coarse resolution of our global model.

In the phosphorus cycle Equations A1–A3, k_{dP} is an optimizable parameter defining the remineralization rate of DOP; κ_p is a fixed particle dissolution rate constant (this parameter also appears in the sinking velocity expression); and κ_g is a slow geologic restoring rate. The geologic restoring term ensures a reasonable integrated total DIP in the model by slowly restoring model [DIP] to the volume-weighted global average of the gridded GLODAPv2 observations ($\langle [DIP]_{obs} \rangle$).

Both the $\mathbf{T}$ and $\mathbf{S}_{POP}$ are formulated in terms of sparse matrices. At steady-state the time-derivatives in Equations A1–A3 vanish. The resulting system of linear equations can be expressed in matrix form and solved efficiently by direct matrix inversion.

The carbon cycle model includes five tracers, dissolved inorganic carbon (DIC), dissolved organic carbon (DOC), particulate organic carbon (POC), as well as particulate inorganic carbon (PIC) in the form of calcium carbonate, and alkalinity (ALK), plus an optional atmospheric pCO_2 variable.

$$\left[\frac{d}{dt} + \mathbf{T}\right][\mathrm{DIC}] = -R_{\mathrm{rain}}\mathbf{\Gamma}R_{C:P} + \kappa_{dC}[\mathrm{DOC}] + \kappa_{\mathrm{PIC}}[\mathrm{PIC}] + \mathbf{F}_{\mathrm{CO_2}} + \mathbf{F}_{v\mathrm{DIC}}\overline{[\mathrm{DIC}]}_s \tag{A7}$$

$$\left[\frac{d}{dt} + \mathbf{T}\right][\mathrm{ALK}] = -2R_{\mathrm{rain}}\mathbf{\Gamma}R_{C:P} + R_{\mathrm{N:C}}\mathbf{\Gamma}R_{C:P} - R_{\mathrm{N:C}}\kappa_{dC}[\mathrm{DOC}] + 2\kappa_{\mathrm{PIC}}[\mathrm{PIC}] + \kappa_g\left([\mathrm{ALK}] - \langle [\mathrm{ALK}]_{\mathrm{obs}} \rangle\right) - \mathbf{F}_{v\mathrm{ALK}}\overline{[\mathrm{ALK}]}_s \tag{A8}$$

$$\left[\frac{d}{dt} + \mathbf{T}\right][\mathrm{DOC}] = -\kappa_{dC}[\mathrm{DOC}] + \kappa_p[\mathrm{POC}] \tag{A9}$$

$$\left[\frac{d}{dt} + \mathbf{S}_{\mathrm{POC}}\right][\mathrm{POC}] = \mathbf{\Gamma}R_{C:P} - \kappa_p[\mathrm{POC}] \tag{A10}$$

$$\left[\frac{d}{dt} + \mathbf{S}_{\mathrm{PIC}}\right][\mathrm{PIC}] = R_{\mathrm{rain}}\mathbf{\Gamma}R_{C:P} - \kappa_{\mathrm{PIC}}[\mathrm{PIC}] \tag{A11}$$

$$\frac{d}{dt}[p\mathrm{CO}_{2,\mathrm{atm}}] = -(\mathbf{F}_{\mathrm{CO_2}}V/N_{\mathrm{atm}})\,10^3 + \kappa_g\left([\mathrm{C_{Total}}] - [\mathrm{C_{Total}}]_{\mathrm{opt}}\right)/N_{\mathrm{atm}} \tag{A12}$$

$\mathbf{\Gamma}$ denotes the biological production of organic phosphorous ($\mathbf{\Gamma} = \gamma[DIP]$), which is converted to the production of organic carbon using the C to P stoichiometric ratio $R_{C:P}$. The production of PIC is proportional to the POC production, using an optimizable parameter, R_{rain}, for the ratio of $CaCO_3$ to POC production (the rain ratio).

Alkalinity is produced by the dissolution of PIC, and consumed by PIC production, with 2 mol of alkalinity produced for every mole of PIC dissolved ($2\kappa_{\mathrm{PIC}}[\mathrm{PIC}]$) , and 2 mol of alkalinity consumed for every mole of PIC produced ($-2R_{\mathrm{rain}}\mathbf{\Gamma}R_{C:P} + R_{\mathrm{N:C}}\mathbf{\Gamma}R_{C:P}$). The $R_{\mathrm{N:C}}$ term in Equation A8 is a fixed nitrogen to carbon ratio for organic matter. This is used because POC production increases alkalinity by changing the chemical form of nitrogen. For the same reason, DOC remineralization decreases alkalinity.

The transport operators for particulate organic and inorganic carbon, $\mathbf{S}_{POC}$ and $\mathbf{S}_{PIC}$ are defined such that

$$\mathbf{S}_{\mathrm{POC}}[\mathrm{POC}] = \nabla \cdot (\mathbf{w}_{\mathrm{POC}}[\mathrm{POC}]), \tag{A13}$$

and

$$\mathbf{S}_{\mathrm{PIC}}[\mathrm{PIC}] = \nabla \cdot (\mathbf{w}_{\mathrm{PIC}}[\mathrm{PIC}]), \tag{A14}$$

where $\mathbf{w}_{\mathrm{POC}} = w(z)_{\mathrm{POC}}\hat{\mathbf{z}}$ is the sinking speed of the particles with $w(z) = -(\kappa_p/b_C)z$. The power-law exponent b_C plays the same role as b_P except for organic carbon instead of organic phosphorus. The sinking speed for PIC is assumed constant, $\mathbf{w}_{\mathrm{PIC}} = -d \cdot \kappa_{\mathrm{PIC}}\hat{\mathbf{z}}$, so that the PIC flux decays exponentially with a length scale d.

Globally uniform parameters control the remineralization rate of DOM. These are k_{dP} for DOP and k_{dC} for DOC. Both k_{dP} and k_{dC} are optimizable parameters. Globally uniform parameters also control the dissolution rates of POM (κ_p) and PIC (κ_{PIC}). Both κ_p and κ_{PIC} are prescribed parameters set to produce e-folding dissolution timescales of 30 days.

Assuming a steady-state, the carbon-cycle equations reduce to a system of non-linear algebraic equations that can be solved iteratively using Newton's method. The value of [DIP] is held fixed at the value obtained by solving the steady-state phosphorus-cycle model. For the case of the preindustrial steady-state, the last equation for the atmospheric $p\mathrm{CO}_2$ can be eliminated by holding the atmospheric CO_2 fixed at a value of 278 ppm. For the case of a future steady-state, we hold the total amount of carbon in the ocean-atmosphere system fixed and use Equation A12 to solve for $p\mathrm{CO}_2$.

The carbon cycle equilibrium solver has an additional optional constraint equation, which is not implemented when optimizing the model, but is used to solve the future equilibrium scenario. This equation solves for atmospheric $p\mathrm{CO}_2$ assuming a fixed amount of carbon in the combined ocean-atmosphere system.

A slow restoring term with a timescale of $1/\kappa_g = 10^6$ years is used to set the total amount of phosphorus, alkalinity, and carbon. The restoring term in the optional $p\mathrm{CO}_2$ equation is defined as the difference between the prescribed total carbon in the system and the sum of carbon in the DIC, DOC, POC, and PIC pools converted to a partial pressure of CO_2 in the atmosphere multiplied by a very small restoring rate. This is analogous to the restoring term in the DIP equation in the phosphorus cycle equilibrium model, and uses the same geologic timescale (k_g). The restoring term in the optional $p\mathrm{CO}_2$ equation is written as,

$$\kappa_g\left([\mathrm{C}_{\mathrm{Total}}] - [\mathrm{C}_{\mathrm{Total}}]_{\mathrm{opt}}\right) 10^6/N_{\mathrm{atm}}$$

where $[\mathrm{C}_{\mathrm{Total}}]$ is the total amount of carbon in the system in units of moles C. N_{atm} is the molar volume of the atmosphere, which we hold fixed at a value of 1.773×10^{20} mol. The conversion factor of 10^6 converts moles C to μmol C to yield the CO_2 concentration in ppm. The prescribed total carbon in the system is defined as the total moles of carbon in the system calculated from the optimized preindustrial steady state model solution $\left([\mathrm{C}_{\mathrm{Total}}]_{\mathrm{opt}}\right)$. $[\mathrm{C}_{\mathrm{Total}}]$ is calculated as:

$$[\mathrm{C}_{\mathrm{Total}}] = ([\mathrm{DIC}] + [\mathrm{POC}] + [\mathrm{DOC}] + [\mathrm{PIC}])' \cdot V 10^{-3} + \left[p\mathrm{CO}_{2,\mathrm{atm}}\right] N_{\mathrm{atm}} 10^{-6}$$

where V is a vector of model grid cell volumes in units of m^3. The dot product computes the global integral. The concentrations of DIC, DOC, POC, and PIC are in units of $\mathrm{mmol/m}^3$. The factor of 10^{-3} converts mmol to moles C.

The carbon cycle is also influenced by sea-surface fluxes, including both air-sea gas exchange ($\mathbf{F}_{\mathrm{CO}_2}$) and the concentrating and diluting effects of evaporation and precipitation on DIC and alkalinity ($\mathbf{F}_{v\mathrm{DIC}}\overline{[\mathrm{DIC}]}_s$ and $\mathbf{F}_{v\mathrm{ALK}}\overline{[\mathrm{ALK}]}_s$ where $\overline{[\mathrm{DIC}]}_s$ and $\overline{[\mathrm{ALK}]}_s$ are mean surface concentrations). The gas transfer term is expressed as,

$$\mathbf{F}_{\mathrm{CO}_2} = \frac{k_w}{\Delta z_1}\left([\mathrm{CO}_2]_{\mathrm{sat}} - [\mathrm{CO}_2]_{\mathrm{surf}}\right), \tag{A15}$$

where $\Delta z_1 = 36$ m is the thickness of the surface layer in the model. $[\mathrm{CO}_2]_{\mathrm{surf}}$ is the aqueous CO_2 concentration at the sea surface in μmol/kg, computed from the modeled surface DIC and ALK using CO2SYS (Lewis et al., 1998; Van Heuven et al., 2011). The saturated aqueous CO_2 concentration, $[\mathrm{CO}_2]_{\mathrm{sat}}$, is computed by multiplying the atmospheric $p\mathrm{CO}_2$ (in μatm) with the solubility of CO_2 in seawater k_0 (in $\mathrm{mol\ kg^{-1}\ atm^{-1}}$). k_w is the air-sea CO_2 transfer velocity, formulated following the second phase of the Ocean Carbon Model Intercomparison Project (OCMIP2) protocol (Najjar et al., 2007) and is based on the parameterization of Wanninkhof (1992).

Appendix B: Fixed Parameters

Descriptions and values of all fixed parameters used in the mechanistic cellular growth model are listed in Table B1.

Table B1
Descriptions, Values, and Units of Fixed Model Parameters in the Mechanistic Cellular Growth Model

Symbol	Value	Units	Description
γ_{DNA}	0.016		DNA fraction of cell
γ_{Lipid}	0.173		Structural Lipid (non-membrane or periplasm) fraction of cell
D_{N_0}	1.296×10^{-6}	m^2/hr	Diffusivity of Nitrate at 25°C
D_{P_0}	1.296×10^{-6}	m^2/hr	Diffusivity of Phosphate at 25°C
$Q_{10}^{Diffusivity}$	1.5		Q10 temperature dependence of diffusivity
Q_{10}^{Bio}	2.0		Q10 temperature dependence of biosynthesis
A_{min}	0.05		Minimal fraction of cell dry mass that is nutrient uptake proteins
Φ_S	0.67	gC/gC	Specific carbon cost of synthesizing functional organic material
p_{Dry}	0.47		Dry mass fraction of the cell
ρ_{cell}	1×10^{-12}	g/μm^3	Cell density
α_{Rib}^{E}	0.60		Mass fraction of the biosynthetic apparatus devoted to ribosomes
α_{PLip}^{M}	0.12		Mass fraction of cell membrane devoted to phospholipids
α_{Prot}^{M}	0.25		Mass fraction of cell membrane devoted to proteins
α_{Prot}^{L}	0.7		Mass fraction of light harvesting apparatus devoted to proteins
β_{stor}	2	μm^{-1}	Logistic growth rate in Equation 13
f_{plip}	0.185		Scale factor for maximum phospholipid quota in Equation 12
$[DIP]_0^{plip}$	1	mmol m^{-3}	DIP threshold for phospholipid substitution (inflection point of logistic function in Equation 12)
β_{plip}	3	$m^3 mmol^{-1}$	Logistic growth rate in Equation 12
P_{DNA}	0.095	gP/g	Phosphorus mass fraction in DNA
P_{Rib}	0.047	gP/g	Phosphorus mass fraction in ribosomes
P_{Plipid}	0.042	gP/g	Phosphorus mass fraction in phospholipids
N_{Prot}	0.16	gN/g	Nitrogen mass fraction in proteins
N_{DNA}	0.16	gN/g	Nitrogen mass fraction in DNA
N_{Rib}	0.16	gN/g	Nitrogen mass fraction in Ribosomes
C_{Prot}	0.53	gC/g	Carbon mass fraction in proteins
C_{DNA}	0.36	gC/g	Carbon mass fraction in DNA
C_{Plipid}	0.65	gC/g	Carbon mass fraction in phospholipids
C_{Lipid}	0.76	gC/g	Carbon mass fraction in other lipids
C_{Rib}	0.419	gC/g	Carbon mass fraction in ribosomes

Data Availability Statement

The global database for temperature, phosphate, and nitrate input in the biogeochemical model are from the World Ocean Atlas 2013 and available at https://www.nodc.noaa.gov/cgi-bin/OC5/woa13/woa13.pl (H. E. Garcia et al., 2014; Locarnini et al., 2013). The net primary productivity data (for Equation A6) are calculated from the Carbon-based Productivity Model, described in Westberry et al. (2008) and available at http://sites.science.oregonstate.edu/ocean.productivity. Surface PAR data is available from the NASA ocean color level 3 browser: https://oceancolor.gsfc.nasa.gov/l3/ (NASA, 2018). SeaWiFS 9 km mission composite is interpolated to our model grid using Matlab's `interp2` function. Euphotic zone light levels input in the cellular growth model are computed by vertically averaging PAR over the grid box, assuming an e-folding depth of 25 m. The global

database for phosphate, alkalinity and dissolved inorganic carbon used in the optimization objective function are from Olsen et al. (2016) and available at https://www.ncei.noaa.gov/access/ocean-carbon-acidification-data-system/oceans/GLODAPv2/. The dissolved organic carbon data used in the optimization objective function are from Letscher and Moore (2015). *Code Availability Statement*: The model code, output, and preprocessed input data sets supporting this paper are available at https://doi.org/10.6084/m9.figshare.24203388 (Sullivan et al., 2024).

Acknowledgments
This study was supported by the U.S. National Science Foundation (OCE-1848576 and OCE-1948842 to A.C.M. and F.W.P., OCE-2124014 to F.W.P., and IOS-2137340 to G.I.H.), the National Oceanic and Atmospheric Administration (NOAA) (Grant NA18OAR4320123 to G.I.H), the Miller Family Foundation (to G.I.H), and the Natural Science Foundation of Fujian Province of China (2023J02001 to W.W.).

References

Clark, J. R., Daines, S. J., Lenton, T. M., Watson, A. J., & Williams, H. T. (2011). Individual-based modelling of adaptation in marine microbial populations using genetically defined physiological parameters. *Ecological Modelling*, *222*(23–24), 3823–3837. https://doi.org/10.1016/J.ECOLMODEL.2011.10.001

Clark, J. R., Lenton, T. M., Williams, H. T., & Daines, S. J. (2013). Environmental selection and resource allocation determine spatial patterns in picophytoplankton cell size. *Limnology & Oceanography*, *58*(3), 1008–1022. https://doi.org/10.4319/lo.2013.58.3.1008

Daines, S. J., Clark, J. R., & Lenton, T. M. (2014). Multiple environmental controls on phytoplankton growth strategies determine adaptive responses of the N:P ratio. *Ecology Letters*, *17*(4), 414–425. https://doi.org/10.1111/ele.12239

DeVries, T., & Holzer, M. (2019). Radiocarbon and helium isotope constraints on deep ocean ventilation and mantle-^{3}He sources. *Journal of Geophysical Research: Oceans*, *124*(5), 3036–3057. https://doi.org/10.1029/2018JC014716

DeVries, T., & Primeau, F. (2011). Dynamically and observationally constrained estimates of water-mass distributions and ages in the global ocean. *Journal of Physical Oceanography*, *41*(12), 2381–2401. https://doi.org/10.1175/JPO-D-10-05011.1

DeVries, T., & Weber, T. (2017). The export and fate of organic matter in the ocean: New constraints from combining satellite and oceanographic tracer observations. *Global Biogeochemical Cycles*, *31*(3), 535–555. https://doi.org/10.1002/2016GB005551

Franks, P. J. (2009). Planktonic ecosystem models: Perplexing parameterizations and a failure to fail. *Journal of Plankton Research*, *31*(11), 1299–1306. https://doi.org/10.1093/PLANKT/FBP069

Fu, W., & Wang, W.-L. (2022). Biogeochemical equilibrium responses to maximal productivity in high nutrient low chlorophyll regions. *Journal of Geophysical Research: Biogeosciences*, *127*(5), e2021JG006636. https://doi.org/10.1029/2021JG006636

Galbraith, E. D., & Martiny, A. C. (2015). A simple nutrient-dependence mechanism for predicting the stoichiometry of marine ecosystems. *Proceedings of the National Academy of Sciences of the United States of America*, *112*(27), 8199–8204. https://doi.org/10.1073/pnas.1423917112

Garcia, C. A., Hagstrom, G. I., Larkin, A. A., Ustick, L. J., Levin, S. A., Lomas, M. W., & Martiny, A. C. (2020). Linking regional shifts in microbial genome adaptation with surface ocean biogeochemistry. *Philosophical Transactions of the Royal Society B: Biological Sciences*, *375*(1798), 20190254. https://doi.org/10.1098/rstb.2019.0254

Garcia, H. E., Locarnini, R. A., Boyer, T. P., Antonov, J. I., Baranova, O. K., Zweng, M. M., et al. (2014). *World Ocean Atlas 2013 volume 4: Dissolved inorganic nutrients (phosphate, nitrate, silicate)*. In S. Levitus, & A. Mishonov (Eds.), (p. 25). NOAA Atlas NESDIS 76. https://doi.org/10.7289/V5J67DWD

Geider, R. J., & La Roche, J. (2002). Redfield revisited: Variability of C:N:P in marine microalgae and its biochemical basis. *European Journal of Phycology*, *37*, 1–17. https://doi.org/10.1017/S0967026201003456

Hagstrom, G. I., & Levin, S. A. (2017). Marine ecosystems as complex adaptive systems: Emergent patterns, critical transitions, and public goods. *Ecosystems*, *20*(3), 458–476. https://doi.org/10.1007/s10021-017-0114-3

Henson, S. A., Laufkötter, C., Leung, S., Giering, S. L., Palevsky, H. I., & Cavan, E. L. (2022). Uncertain response of ocean biological carbon export in a changing world. *Nature Geoscience*, *15*(4), 248–254. https://doi.org/10.1038/s41561-022-00927-0

Inomura, K., Omta, A. W., Talmy, D., Bragg, J., Deutsch, C., & Follows, M. J. (2020). A mechanistic model of macromolecular allocation, elemental stoichiometry, and growth rate in phytoplankton. *Frontiers in Microbiology*, *11*, 86. https://doi.org/10.3389/fmicb.2020.00086

Kelley, C. T. (2003). *Solving nonlinear equations with Newton's method*. Society for Industrial and Applied Mathematics. https://doi.org/10.1137/1.9780898718898

Kiørboe, T., Visser, A., & Andersen, K. H. (2018). A trait-based approach to ocean ecology. *ICES Journal of Marine Science*, *75*(6), 1849–1863. https://doi.org/10.1093/icesjms/fsy090

Kwiatkowski, L., Aumont, O., Bopp, L., & Ciais, P. (2018). The impact of variable phytoplankton stoichiometry on projections of primary production, food quality, and carbon uptake in the global ocean. *Global Biogeochemical Cycles*, *32*(4), 516–528. https://doi.org/10.1002/2017GB005799

Kwiatkowski, L., Torres, O., Bopp, L., Aumont, O., Chamberlain, M., Christian, J. R., et al. (2020). Twenty-first century ocean warming, acidification, deoxygenation, and upper-ocean nutrient and primary production decline from CMIP6 model projections. *Biogeosciences*, *17*(13), 3439–3470. https://doi.org/10.5194/BG-17-3439-2020

Kwon, E. Y., Holzer, M., Timmermann, A., & Primeau, F. (2022a). Estimating three-dimensional carbon-to-phosphorus stoichiometry of exported marine organic matter. *Global Biogeochemical Cycles*, *36*(3). https://doi.org/10.1029/2021GB007154

Kwon, E. Y., Sreeush, M. G., Timmermann, A., Karl, D. M., Church, M. J., Lee, S.-S., & Yamaguchi, R. (2022b). Nutrient uptake plasticity in phytoplankton sustains future ocean net primary production. *Science Advances*, *8*(51), eadd2475. https://doi.org/10.1126/sciadv.add2475

Letscher, R. T., & Moore, J. K. (2015). Preferential remineralization of dissolved organic phosphorus and non-Redfield DOM dynamics in the global ocean: Impacts on marine productivity, nitrogen fixation, and carbon export. *Global Biogeochemical Cycles*, *29*(3), 325–340. https://doi.org/10.1002/2014GB004904

Letscher, R. T., & Moore, J. K. (2017). Modest net autotrophy in the oligotrophic ocean. *Global Biogeochemical Cycles*, *31*(4), 699–708. https://doi.org/10.1002/2016GB005503

Lewis, E., Wallace, D., & Allison, L. J. (1998). Program developed for CO_2 system calculations. https://doi.org/10.2172/639712

Liefer, J. D., Garg, A., Fyfe, M. H., Irwin, A. J., Benner, I., Brown, C. M., et al. (2019). The macromolecular basis of phytoplankton C:N:P under nitrogen starvation. *Frontiers in Microbiology*, *10*, 763. https://doi.org/10.3389/FMICB.2019.00763

Lin, S., Litaker, R. W., & Sunda, W. G. (2016). Phosphorus physiological ecology and molecular mechanisms in marine phytoplankton. *Journal of Phycology*, *52*(1), 10–36. https://doi.org/10.1111/JPY.12365

Litchman, E., & Klausmeier, C. A. (2008). Trait-based community ecology of phytoplankton. *Annual Review of Ecology, Evolution, and Systematics*, *39*(1), 615–639. https://doi.org/10.1146/annurev.ecolsys.39.110707.173549

Locarnini, R. A., Mishonov, A. V., Antonov, J. I., Boyer, T. P., Garcia, H. E., Baranova, O. K., et al. (2013). *World Ocean Atlas 2013 volume 1: Temperature*. In S. Levitus, & A. Mishonov (Eds.), (p. 40). NOAA Atlas NESDIS 73. https://doi.org/10.7289/V55X26VD

Lomas, M. W., Bates, N. R., Johnson, R. J., Steinberg, D. K., & Tanioka, T. (2022). Adaptive carbon export response to warming in the Sargasso Sea. *Nature Communications*, *13*(1), 1211. https://doi.org/10.1038/s41467-022-28842-3

Long, M. C., Moore, J. K., Lindsay, K., Levy, M., Doney, S. C., Luo, J. Y., et al. (2021). Simulations with the marine biogeochemistry library (MARBL). *Journal of Advances in Modeling Earth Systems*, *13*(12), e2021MS002647. https://doi.org/10.1029/2021MS002647

Marsay, C. M., Sanders, R. J., Henson, S. A., Pabortsava, K., Achterberg, E. P., & Lampitt, R. S. (2015). Attenuation of sinking particulate organic carbon flux through the mesopelagic ocean. *Proceedings of the National Academy of Sciences of the United States of America*, *112*(4), 1089–1094. https://doi.org/10.1073/pnas.1415311112

Martin, P., & Van Mooy, B. A. (2013). Fluorometric quantification of polyphosphate in environmental plankton samples: Extraction protocols, matrix effects, and nucleic acid interference. *Applied and Environmental Microbiology*, *79*(1), 273–281. https://doi.org/10.1128/AEM.02592-12

Martiny, A. C., Pham, C. T., Primeau, F. W., Vrugt, J. A., Moore, J. K., Levin, S. A., & Lomas, M. W. (2013). Strong latitudinal patterns in the elemental ratios of marine plankton and organic matter. *Nature Geoscience*, *6*(4), 279–283. https://doi.org/10.1038/ngeo1757

Meinshausen, M., Nicholls, Z. R., Lewis, J., Gidden, M. J., Vogel, E., Freund, M., et al. (2020). The shared socio-economic pathway (SSP) greenhouse gas concentrations and their extensions to 2500. *Geoscientific Model Development*, *13*(8), 3571–3605. https://doi.org/10.5194/GMD-13-3571-2020

Meinshausen, M., Vogel, E., Nauels, A., Lorbacher, K., Meinshausen, N., Etheridge, D. M., et al. (2017). Historical greenhouse gas concentrations for climate modelling (CMIP6). *Geoscientific Model Development*, *10*(5), 2057–2116. https://doi.org/10.5194/GMD-10-2057-2017

Moore, J. K., Lindsay, K., Doney, S. C., Long, M. C., & Misumi, K. (2013). Marine ecosystem dynamics and biogeochemical cycling in the community Earth system model [CESM1(BGC)]: Comparison of the 1990s with the 2090s under the RCP4.5 and RCP8.5 scenarios. *Journal of Climate*, *26*(23), 9291–9312. https://doi.org/10.1175/JCLI-D-12-00566.1

Moreno, A. R., Hagstrom, G. I., Primeau, F. W., Levin, S. A., & Martiny, A. C. (2018). Marine phytoplankton stoichiometry mediates nonlinear interactions between nutrient supply, temperature, and atmospheric CO_2. *Biogeosciences*, *15*(9), 2761–2779. https://doi.org/10.5194/bg-15-2761-2018

Moreno, A. R., & Martiny, A. C. (2018). Ecological stoichiometry of ocean plankton. *Annual Review of Marine Science*, *10*(1), 43–69. https://doi.org/10.1146/annurev-marine-121916-063126

Najjar, R. G., Jin, X., Louanchi, F., Aumont, O., Caldeira, K., Doney, S. C., et al. (2007). Impact of circulation on export production, dissolved organic matter, and dissolved oxygen in the ocean: Results from phase II of the ocean carbon-cycle model intercomparison project (OCMIP-2). *Global Biogeochemical Cycles*, *21*(3), 3007. https://doi.org/10.1029/2006GB002857

NASA Ocean Biology Processing Group. (2018). SeaWiFS-OrbView-2 level 3 mapped photosynthetically available radiation data version r2018.0 [Dataset]. NASA Ocean Biology Distributed Active Archive Center. https://doi.org/10.5067/ORBVIEW-2/SEAWIFS/L3M/PAR/2018

National Academies of Sciences, Engineering, and Medicine. (2022). *A research strategy for ocean-based carbon dioxide removal and sequestration*. The National Academies Press. https://doi.org/10.17226/26278

Nowicki, M., DeVries, T., & Siegel, D. A. (2022). Quantifying the carbon export and sequestration pathways of the ocean's biological carbon pump. *Global Biogeochemical Cycles*, *36*(3), e2021GB007083. https://doi.org/10.1029/2021GB007083

Olsen, A., Key, R. M., Heuven, S. V., Lauvset, S. K., Velo, A., Lin, X., et al. (2016). The global ocean data analysis project version 2 (GLODAPv2)—An internally consistent data product for the world ocean. *Earth System Science Data*, *8*, 297–323. https://doi.org/10.5194/essd-8-297-2016

Orchard, E. D., Benitez-Nelson, C. R., Pellechia, P. J., Lomas, M. W., & Dyhrman, S. T. (2010). Polyphosphate in *Trichodesmium* from the low-phosphorus Sargasso Sea. *Limnology & Oceanography*, *55*(5), 2161–2169. https://doi.org/10.4319/LO.2010.55.5.2161

Primeau, F. W., Holzer, M., & DeVries, T. (2013). Southern ocean nutrient trapping and the efficiency of the biological pump. *Journal of Geophysical Research: Oceans*, *118*(5), 2547–2564. https://doi.org/10.1002/jgrc.20181

Raven, J. A., & Geider, R. J. (1988). Temperature and algal growth. *New Phytologist*, *110*(4), 441–461. https://doi.org/10.1111/J.1469-8137.1988.TB00282.X

Redfield, A. C. (1934). On the proportions of organic derivatives in sea water and their relation to the composition of plankton. *James Johnstone Memorial*, 176–192.

Redfield, A. C. (1958). The biological control of chemical factors in the environment. *American Scientist*, *46*, 205–221. Retrieved from https://www.jstor.org/stable/27827150

Séférian, R., Berthet, S., Yool, A., Palmiéri, J., Bopp, L., Tagliabue, A., et al. (2020). Tracking improvement in simulated marine biogeochemistry between CMIP5 and CMIP6. *Current Climate Change Reports*, *6*(3), 95–119. https://doi.org/10.1007/s40641-020-00160-0

Shuter, B. (1979). A model of physiological adaptation in unicellular algae. *Journal of Theoretical Biology*, *78*(4), 519–552. https://doi.org/10.1016/0022-5193(79)90189-9

Siegel, D. A., Buesseler, K. O., Doney, S. C., Sailley, S. F., Behrenfeld, M. J., & Boyd, P. W. (2014). Global assessment of ocean carbon export by combining satellite observations and food-web models. *Global Biogeochemical Cycles*, *28*(3), 181–196. https://doi.org/10.1002/2013GB004743

Sigman, D. M., & Boyle, E. A. (2000). Glacial/interglacial variations in atmospheric carbon dioxide. *Nature*, *407*(6806), 859–869. https://doi.org/10.1038/35038000

Smith, S. L., Pahlow, M., Merico, A., & Wirtz, K. W. (2011). Optimality-based modeling of planktonic organisms. *Limnology & Oceanography*, *56*(6), 2080–2094. https://doi.org/10.4319/LO.2011.56.6.2080

Sullivan, M., Primeau, F., Hagstrom, G. I., Wang, W.-L., & Martiny, A. C. (2024). Phytoplankton carbon-to-phosphorus in a biogeochemical inverse model [Dataset]. figshare. https://doi.org/10.6084/m9.figshare.24203388

Tanioka, T., Garcia, C. A., Larkin, A. A., Garcia, N. S., Fagan, A. J., & Martiny, A. C. (2022). Global patterns and predictors of C:N:P in marine ecosystems. *Communications Earth & Environment*, *3*, 1–9. https://doi.org/10.1038/s43247-022-00603-6

Tanioka, T., Larkin, A. A., Moreno, A. R., Brock, M. L., Fagan, A. J., Garcia, C. A., et al. (2022). Global ocean particulate organic phosphorus, carbon, oxygen for respiration, and nitrogen (GO-POPCORN) [Dataset]. Scientific Data, *9*(1), 688. https://doi.org/10.1038/s41597-022-01809-1

Tanioka, T., & Matsumoto, K. (2017). Buffering of ocean export production by flexible elemental stoichiometry of particulate organic matter. *Global Biogeochemical Cycles*, *31*(10), 1528–1542. https://doi.org/10.1002/2017GB005670

Tanioka, T., Matsumoto, K., & Lomas, M. W. (2021). Drawdown of atmospheric pCO_2 via variable particle flux stoichiometry in the ocean twilight zone. *Geophysical Research Letters*, *48*(22), e2021GL094924. https://doi.org/10.1029/2021GL094924

Teng, Y. C., Primeau, F. W., Moore, J. K., Lomas, M. W., & Martiny, A. C. (2014). Global-scale variations of the ratios of carbon to phosphorus in exported marine organic matter. *Nature Geoscience*, *7*(12), 895–898. https://doi.org/10.1038/ngeo2303

Toseland, A., Daines, S. J., Clark, J. R., Kirkham, A., Strauss, J., Uhlig, C., et al. (2013). The impact of temperature on marine phytoplankton resource allocation and metabolism. *Nature Climate Change*, *3*(11), 979–984. https://doi.org/10.1038/nclimate1989

Van Heuven, S., Pierrot, D., Rae, J. W. B., Lewis, E., & Wallace, D. W. R. (2011). *Matlab program developed for CO_2 system calculations (Computer program No. ORNL/CDIAC-105b)*. Oak Ridge, Tennessee: Carbon Dioxide Information Analysis Center, Oak Ridge National Laboratory, U.S. Department of Energy.

Van Mooy, B. A. S., Fredricks, H. F., Pedler, B. E., Dyhrman, S. T., Karl, D. M., Koblížek, M., et al. (2009). Phytoplankton in the ocean use non-phosphorus lipids in response to phosphorus scarcity. *Nature*, *458*(7234), 69–72. https://doi.org/10.1038/nature07659

Wang, W.-L., Fu, W., Moigne, F. A. C. L., Letscher, R. T., Liu, Y., Tang, J.-M., & Primeau, F. W. (2023). Biological carbon pump estimate based on multidecadal hydrographic data. *Nature*, *624*(7992), 579–585. https://doi.org/10.1038/s41586-023-06772-4

Wang, W. L., Moore, J. K., Martiny, A. C., & Primeau, F. W. (2019). Convergent estimates of marine nitrogen fixation. *Nature*, *566*(7743), 205–211. https://doi.org/10.1038/s41586-019-0911-2

Wanninkhof, R. (1992). Relationship between wind speed and gas exchange over the ocean. *Journal of Geophysical Research*, *97*(C5), 7373–7382. https://doi.org/10.1029/92JC00188

Westberry, T., Behrenfeld, M. J., Siegel, D. A., & Boss, E. (2008). Carbon-based primary productivity modeling with vertically resolved photoacclimation. *Global Biogeochemical Cycles*, *22*(2), 2024. https://doi.org/10.1029/2007GB003078

Yvon-Durocher, G., Dossena, M., Trimmer, M., Woodward, G., & Allen, A. P. (2015). Temperature and the biogeography of algal stoichiometry. *Global Ecology and Biogeography*, *24*(5), 562–570. https://doi.org/10.1111/geb.12280